

# Densely Sampled Global Dynamic Topographic Observations and Their Significance

M.C. Holdt<sup>1</sup>, N.J. White<sup>1</sup>, S.N. Stephenson<sup>2</sup> and B.W. Conway-Jones<sup>1</sup>

<sup>1</sup>Bullard Laboratories, Department of Earth Sciences, University of Cambridge, Madingley Rise,  
Madingley Road, Cambridge, CB3 0EZ, UK

<sup>2</sup>Department of Earth Sciences, University of Oxford, South Parks Road, Oxford, OX1 3AN, UK

## Key Points:

- 7,601 seismic profiles yield residual depth measurements throughout the oceanic realm.
- Spherical harmonic representations of dynamic topography are generated from combined oceanic and continental measurements.
- Resultant power spectra are consistent with Stokes' flow of convecting mantle.

---

Corresponding author: M.C. Holdt, N.J. White, [mch74@cam.ac.uk](mailto:mch74@cam.ac.uk), [njw10@cam.ac.uk](mailto:njw10@cam.ac.uk)

**Abstract**

Topography and bathymetry are principally supported by some combination of crustal and sub-crustal density variations. However, dynamic topography is generated by vertical deflection of the Earth's surface as a result of mantle convection. Isolating and quantifying observable dynamic topography yields valuable information about mantle processes. Here, we investigate global dynamic topography by calculating residual depth anomalies throughout the oceanic realm and residual topographic anomalies across the continents. We correct for sedimentary and crustal loading by exploiting a variety of seismicologic datasets that include seismic reflection profiles, wide-angle/refraction surveys and receiver functions. In this way, an extensively revised and augmented global compilation of 10,874 oceanic residual depth measurements and 3,777 continental residual topographic measurements is constructed. In the oceanic realm, the methodology has been revised to improve accuracy and resolution. First, quartz/clay content of the sedimentary column is adjusted to remove minor skewness of residual depth anomalies as a function of plate age. Secondly, variation of bulk density as a function of crustal thickness is taken into account. Our global compilation is used to generate spherical harmonic representations of observable dynamic topography out to degree 40 (i.e.  $\sim 1000$  km). Resultant spectra demonstrate that dynamic topographic power varies linearly with inverse wavenumber. The spectral slope directly reflects the way by which dynamic topography is generated by Stokes' flow. Our global results are consistent with independent and diverse geologic markers of uplift and subsidence together with Neogene-Quaternary intraplate basalt magmatism.

**Plain Language Summary**

The Earth's surface consists of interlocking tectonic plates that move with respect to each other at rates which we can now observe using the global positioning system. The story of how plate tectonics was discovered in the late 1960s is a very exciting one but the emphasis on horizontal movement of plates has tended to deflect attention away from a significant and related topic. Plate motion must be caused by slow stirring of the Earth's interior and this stirring should also generate lazy up-and-down displacement of the surface we live on. Unfortunately, these vertical movements are probably very slow and so hard to directly measure. In this study, we build upon previous attempts to measure vertical movements across the globe that we think can be attributed to slow stirring of the interior. Our analysis of depth measurements from the oceans and of anomalous topography onshore has enabled us to pinpoint the surface effects of stirring, which appear to occur on a whole host of length scales from hundreds of kilometers to tens of thousands of kilometers.

## 49 1 Introduction

50 It is widely accepted that deflection of the Earth’s surface is generated and main-  
 51 tained by a combination of lithospheric isostasy and sub-lithospheric convective processes.  
 52 Continental topography is dominated by crustal thickness and density variations, although  
 53 changes in lithospheric thickness and density evidently play a contributory role (Pratt,  
 54 1855; Airy, 1855). In contrast, oceanic bathymetry is dominated by cooling and thick-  
 55 ening of the lithospheric plate (Parsons & Sclater, 1977). In both cases, it is agreed that  
 56 some fraction of vertical displacement, referred to as dynamic topography, is attributable  
 57 to density and flow of the underlying mantle (M. A. Richards & Hager, 1984). Thus iso-  
 58 lating and quantifying this dynamic topography, which is expected to vary as a function  
 59 of space and time, should yield significant information about the convective process. This  
 60 task is not straightforward since crustal and lithospheric isostasy dominate the signal.

61 It has long been recognized that the oceanic realm represents an excellent natu-  
 62 ral laboratory for isolating dynamic topography. Oceanic lithosphere appears to be re-  
 63 latively homogeneous and, crucially, it exhibits a predictable relationship between sub-  
 64 sidence and plate age (D. P. McKenzie, 1967; Parsons & Sclater, 1977; Stein & Stein,  
 65 1992; Crosby et al., 2006; F. D. Richards et al., 2018). This age-depth relationship en-  
 66 ables deviations, known as residual depth anomalies, to be identified and measured (Menard,  
 67 1973). The principal difficulty in accurately calculating these anomalies is that hetero-  
 68 geneous sedimentary and crustal loading must be carefully taken into account. Fortu-  
 69 nately, the availability of substantial volumes of high quality seismic reflection and wide-  
 70 angle imagery has dramatically improved our ability to implement both sedimentary and  
 71 crustal corrections with a view to obtaining well-resolved residual depth anomalies (Hoggard  
 72 et al., 2016, 2017).

73 The continental realm represents a much more formidable challenge. Accurate resid-  
 74 ual topographic measurements can be in principal be obtained provided that the den-  
 75 sity structure of both crust and lithosphere are known. Thermal and compositional vari-  
 76 ations caused by protracted geologic histories introduce uncertainty (Jordan, 1975). Since  
 77 the crustal correction dominates, we use a combination of controlled source and passive  
 78 seismic experiments to constrain average crustal density, which enables crustal isostatic  
 79 anomalies to be measured.

80 In this particular contribution, our scientific aims are threefold. First, we present  
 81 an extensively revised and augmented global database of residual measurements, which  
 82 comprises 10,874 residual depth measurements from the oceanic realm and 3,777 resid-  
 83 ual topographic measurements from the continental realm. Secondly, we implement a  
 84 revised methodology for calculating sedimentary and crustal corrections together with  
 85 a modified plate cooling model. In an analogous way, continental measurements were ob-  
 86 tained by correcting local crustal density structure with respect to a global reference crustal  
 87 density structure which sits at mean sea level. Thirdly, we present a revised spherical  
 88 harmonic representation of observed dynamic topography. This representation has been  
 89 extended out to a maximum spherical harmonic degree of 40. The slope of the associ-  
 90 ated power spectrum places important constraints upon the nature of viscous flow within  
 91 the mantle.

## 92 2 A Revised Oceanic Database

93 In his pioneering analysis, Menard (1973) recognized that careful measurement of  
 94 residual bathymetry yields significant information about transient mantle convective pro-  
 95 cesses. Since this seminal contribution, the principal limitation has been the difficulty  
 96 in obtaining high quality measurements of sedimentary and crustal thickness and den-  
 97 sity, which are necessary to obtain accurate residual depth estimates. Hoggard et al. (2016)  
 98 and Hoggard et al. (2017) addressed this limitation by exploiting a combination of mod-

ern seismic reflection surveys, primarily from oceanic lithosphere adjacent to continental margins, and seismic wide-angle/refraction experiments (Figure 1a).

Here, we have considerably expanded this approach with a view to constructing a revised and augmented oceanic database that comprises 1,411 modern (i.e., multi-channel) and 5,444 vintage (i.e., single-channel) seismic reflection profiles, together with 323 modern (i.e., waveform-modeled) seismic wide-angle experiments and 423 vintage (i.e., slope-intercept) seismic refraction experiments (Figure 1b). Locations and sources of these profiles and experiments are documented within the Supporting Information. Hoggard et al. (2017) analyzed a total of 1,725 profiles and experiments. By expanding data sources to include, for example, the Academic Seismic Portal of the Lamont-Doherty Earth Observatory (<https://www.marine-geo.org>), we now analyze a total of 7,601 profiles and experiments.

Our revised and augmented database provides comprehensive coverage throughout the oceanic realm. This coverage is much more evenly distributed than that of Hoggard et al. (2016), whose smaller database is biased toward continental margins where modern high quality seismic reflection surveys that were acquired by industry are concentrated. All the profiles and experiments that we analyze are located upon *bona fide* oceanic crust that is principally identified using a combination of the age model generated by Seton et al. (2020), which we have revised and augmented in places, and magnetic anomalies from the EMAG2 database (Maus et al., 2009). Where magnetic anomalies are less easily interpretable, regional studies of the continent-ocean boundary and the pattern of free-air gravity anomalies are exploited (Sandwell et al., 2014).

Figures 2 and 3 show examples of multi-channel and single-channel seismic reflection profiles, respectively. On modern industry-standard profiles, where long streamers and high fold of cover are employed, oceanic crust is excellently imaged. Critically, both the sediment-basement interface and the Moho are generally crisp and well resolved. These superb images also reveal the detailed internal structure of the sedimentary pile and of the crust. Note that sedimentary and oceanic crustal thicknesses are demonstrably variable. For example, the Gulf of Mexico is characterized by a sedimentary layer of 5 s TWTT and a crustal layer of 1.5 s whereas the Namibian margin has a much thinner sedimentary layer of 1.5 s and a much thicker crustal layer of 2.5 s (compare Figure 2b and e). These measurements are the key to obtaining accurate residual depth anomalies. Although vintage single-channel seismic reflection profiles are inevitably of inferior quality, they do provide critical spatial coverage in the more remote parts of oceanic basins. On significant numbers of these single channel profiles, the seabed and the sediment-basement interface are clearly visible but the Moho discontinuity is rarely, if ever, imaged (e.g., Figure 3c–e).

### 3 Methods

A straightforward method for calculating residual depth anomalies is summarized in Figure 4a. This approach is a moderately revised version of the scheme outlined by Czarnota et al. (2013) and by Hoggard et al. (2017) who, in turn, built upon the original pioneering work of Menard (1973) and of Crough (1983). Residual depth,  $z_r$ , is the difference between the anticipated depth to water-loaded oceanic basement,  $z_w$ , which is calculated from an optimal plate cooling model, and the observed water-loaded depth,  $z_o$ , measured relative to the geoid,  $C_g$ . Thus

$$z_r = z_w - z_o + C_g. \quad (1)$$

Since the thickness and density of the sedimentary layer spatially varies, it is necessary to convert the sedimentary layer into an isostatically equivalent water load,  $C_s$ . Oceanic crustal thickness and density also vary and are taken into account by calculating  $z_o$  with

147 respect to a reference crustal layer, which entails a crustal correction given by  $C_c$ . In this  
 148 way, we obtain

$$z_o = z_{sb} + C_s + C_c, \quad (2)$$

149 where  $z_{sb}$  is the observed water depth. The sedimentary correction,  $C_s$ , is significant and  
 150 must be carried out as carefully and accurately as possible. The crustal correction,  $C_c$ ,  
 151 is of secondary importance. Note that both sedimentary and crustal corrections assume  
 152 Airy isostasy which is a reasonable assumption, given the spatial wavelengths of inter-  
 153 est (Watts, 2001; Hoggard et al., 2017).

### 154 3.1 Sedimentary Correction

155 The sedimentary correction replaces the heterogeneous sedimentary layer, which  
 156 drapes oceanic basement, with an equivalent water load (Figure 4a). This correction,  $C_s$ ,  
 157 is given by

$$C_s = \left( \frac{\rho_a - \bar{\rho}_s}{\rho_a - \rho_w} \right) z_s, \quad (3)$$

158 where  $\rho_a$  is the density of the asthenosphere,  $\bar{\rho}_s$  is the average density of the sedimen-  
 159 tary layer,  $\rho_w$  is the density of water, and  $z_s$  is the thickness of the sedimentary layer  
 160 (see Table 1). For the purposes of this calculation,  $\rho_a$  and  $\rho_w$  are assumed to be constant,  
 161 which means that the spatial variation of  $C_s$  is dependent upon values of  $z_s$  and  $\bar{\rho}_s$ . Both  
 162 values are determined in the following way. Since seismic reflection profiles are acquired  
 163 as a function of two-way travel time, it is essential to convert from time to depth. The  
 164 optimal way to perform this conversion is to exploit coincident seismic reflection and mod-  
 165 ern (i.e., waveform-modeled) seismic wide-angle experiments. Here, we utilize a global  
 166 database of 43 time-depth measurements that was compiled by Winterbourne et al. (2009)  
 167 and revised by Hoggard et al. (2016). These measurements are used to build an empir-  
 168 ical relationship between time and depth (Figure 5).

169 The relationship between depth,  $z$ , and two-way travel time,  $t$ , is

$$t = 2 \int_0^z \frac{dz}{v(z)}, \quad (4)$$

170 where  $v(z)$  is velocity of the sedimentary layer as a function of depth. Since  $v(z)$  varies  
 171 as a function of composition and compaction, we can exploit

$$\frac{1}{v(z)} = \frac{\phi(z)}{v_w} + \frac{1 - \phi(z)}{v_{sg}}, \quad (5)$$

172 where  $v_w$  is velocity of the pore fluid,  $v_{sg}$  is velocity of solid grain material, and  $\phi(z)$  is  
 173 porosity as a function of depth (Wyllie et al., 1956). It is generally accepted that porosity  
 174 decreases with depth according to

$$\phi(z) = \phi_o \exp\left(\frac{-z}{\lambda}\right), \quad (6)$$

175 where  $\phi_o$  is initial porosity and  $\lambda$  is compaction decay length (Athy, 1930). In the ab-  
 176 sence of deeply penetrating boreholes, we assume that this relationship holds for sedi-  
 177 mentary thicknesses that exceed 2 km (Rowley, 2019). By combining Equations 4, 5 and  
 178 6, we obtain

$$\frac{t}{2} = \frac{z}{v_{sg}} + \phi_o \lambda \left( \frac{1}{v_w} - \frac{1}{v_{sg}} \right) \left[ 1 - \exp\left(\frac{-z}{\lambda}\right) \right]. \quad (7)$$

179 In order to constrain values of  $\phi_o$  and  $\lambda$ , the root-mean squared (rms) misfit is cal-  
 180 culated between this  $t$ - $z$  relationship and 43 observed time-depth pairs (Figure 5a). This  
 181 pragmatic approach enables us to conveniently sidestep the paucity of deeply penetrat-  
 182 ing boreholes in the oceanic realm. The misfit space is explored using successive param-  
 183 eter sweeps where  $\phi_o$  is varied between 0 and 1, and where  $\lambda$  is varied between 0 and 10  
 184 for a constant value of  $v_{sg}$ . Optimal values of  $\phi_o = 0.67$  and  $\lambda = 2.3$  km are found at  
 185 the global minimum where the residual rms misfit equals 0.354 (Figure 5b). Uncertainty  
 186 bounds associated with the time-depth curve are calculated by varying  $\phi_o$  and  $\lambda$  to es-  
 187 tablish an envelope that represents one standard deviation where the rms misfit is 0.421.

188 A similar parameter sweep where  $v_{sg}$  is varied is also carried out (Figure 5c-d). How-  
 189 ever,  $v_{sg}$  can vary significantly while still producing a small minimum misfit. Consequently,  
 190 it is preferable to independently determine an optimal value of  $v_{sg}$  using empirical lab-  
 191 oratory measurements. The relationship between p-wave velocity,  $v_p$ , porosity,  $\phi$ , and  
 192 clay fraction,  $C$ , has been obtained for a range of sedimentary samples (Tosaya & Nur,  
 193 1982; Kowallis et al., 1984; Castagna et al., 1985; Han et al., 1986; Eberhart-Phillips et  
 194 al., 1989). These studies show that increasing the clay fraction of sandstones causes  $v_p$   
 195 to systematically decrease. Han et al. (1986) carried out a detailed analysis of 75 sand-  
 196 stone samples and obtained an optimal fit using a least squares regression to velocity mea-  
 197 surements where  $v_p = 5.59 - 6.93\phi - 2.18C$ . For a clay fraction of  $C = 0.5 \pm 0.25$ , this  
 198 empirical relationship is consistent with  $v_{sg} = 4.5 \pm 0.5$  km s<sup>-1</sup>. Note that this esti-  
 199 mate of  $v_{sg}$  is smaller than the value of 5.5 km s<sup>-1</sup> assumed by Hoggard et al. (2017).  
 200 In our view, this slower velocity is more consistent with the fact that abyssal sediments  
 201 are predominantly composed of silty clay.

202 One significant advantage of fitting observed time-depth pairs with a compaction-  
 203 based relationship is that estimating the mean density of the sedimentary layer,  $\bar{\rho}_s$ , is  
 204 straightforward. Since  $\bar{\rho}_s$  depends upon the relative contributions of pore fluid and solid  
 205 grains, we obtain

$$\bar{\rho}_s(z) = \int_0^z \rho_w \phi(z) + \rho_{sg} [1 - \phi(z)] dz \quad (8)$$

206 where  $\rho_{sg}$  is the solid grain density. Combining Equations 8 and 6 yields

$$\bar{\rho}_s(z) = \rho_{sg} + \frac{\phi_o \lambda}{z} (\rho_w - \rho_{sg}) \left[ 1 - \exp\left(\frac{-z}{\lambda}\right) \right]. \quad (9)$$

207 The solid grain density of quartz is  $\rho_{sg} = 2.65 \pm 0.05$  Mg m<sup>-3</sup> (Christensen, 1965).  
 208 Since the solid grain density of typical clay minerals is very similar, we have chosen not  
 209 to vary this parameter (Howie et al., 1992). To calculate solid grain density as a func-  
 210 tion of depth, we use the previously obtained optimal compaction parameters of  $\phi_o =$   
 211 0.67 and  $\lambda = 2.3$  km. The variation of  $\bar{\rho}_s$  as a function of both  $t$  and  $z$  are shown in Fig-  
 212 ure 6a and b, respectively. This variation is consistent with the results of an exhaustive  
 213 global study of bulk sediment densities (Rowley, 2019). In this study, bulk density mea-  
 214 surements were obtained for the upper 1.2 km of the sedimentary layer from 1263 deep-  
 215 sea drilling sites (Figure 6b). These measurements were optimally fitted using  $\phi_o = 0.70$   
 216 and  $\lambda = 2.0$  km in close agreement with our results.

217 The sedimentary correction as a function of  $t$  and  $z$  is shown in Figure 6c and d,  
 218 respectively. This correction is consistent with previously published regional studies that  
 219 are based upon an analysis of boreholes, seismic wide-angle experiments, and core sam-  
 220 ples (Crough, 1983; Sykes, 1996; Louden et al., 2004). Note that our revised sediment-  
 221 ary correction is systematically smaller than that presented by Hoggard et al. (2017).  
 222 This minor difference is a direct consequence of using a smaller (i.e., siltier) value of  $v_{sg}$ ,  
 223 which yields slightly different optimal values of  $\phi_o$  (i.e., 0.67 instead of 0.6) and  $\lambda$  (i.e.,  
 224 2.3 km instead of 3.9 km).

225 The cumulative error arising from uncertainties in parameters used for the sedi-  
 226 mentary correction is not straightforward to propagate. Thus, a *Monte Carlo* scheme is  
 227 exploited. This approach enables the uncertainty envelope for the sedimentary correc-  
 228 tion to be robustly constructed by randomly sampling each parameter value from a Gaus-  
 229 sian distribution, which is based upon the mean and standard deviation of that param-  
 230 eter (Table 1). In this way, the combined uncertainties of compaction parameters, of ve-  
 231 locities, and of densities are propagated.

232 This sedimentary correction is applied to all age-depth measurements from the global  
 233 database presented in Figure 1. This correction is a significant one for regions adjacent  
 234 to continental margins where thick sedimentary sequences occur. In the more remote cor-  
 235 ners of oceanic basins, sedimentary thicknesses are generally less than 1 km which means  
 236 that the correction and its uncertainty is consequently smaller.  $\sim 67\%$  of seismic profiles  
 237 have sedimentary thicknesses  $\leq 0.5$  km and  $\sim 81\%$  of seismic profiles have sedimentary  
 238 thicknesses  $\leq 1$  km, corresponding to isostatic corrections of  $\leq 0.35 \pm 0.04$  km and  $\leq$   
 239  $0.65 \pm 0.06$  km, respectively.  $\sim 95\%$  of seismic profiles have sedimentary thicknesses that  
 240 are  $\leq 3.5$  km, which corresponds to an isostatic correction of  $\leq 1.8 \pm 0.11$  km. Thus the  
 241 bulk of the revised and augmented database yields accurate water-loaded depths to base-  
 242 ment with small uncertainties. Finally, we note that careful interpretation of the sediment-  
 243 basement interface along  $>7000$  seismic reflection profiles yields a significant constraint  
 244 on global sedimentary thickness in more remote oceanic basins (Straume et al., 2019).

### 245 3.2 Crustal Correction

246 A crustal correction,  $C_c$ , adjusts water-loaded depth to basement to allow for the  
 247 fact that locally measured oceanic crustal thickness and its average density,  $z_c$  and  $\bar{\rho}_c$ ,  
 248 are different to mean global crustal thickness and its average density,  $\bar{z}_r$  and  $\bar{\rho}_r$ . By iso-  
 249 statically balancing, we obtain

$$C_c = \left( \frac{\rho_a - \bar{\rho}_c}{\rho_a - \rho_w} \right) z_c - \left( \frac{\rho_a - \bar{\rho}_r}{\rho_a - \rho_w} \right) \bar{z}_r. \quad (10)$$

250 In order to obtain accurate values of  $C_c$ , two forms of analysis are undertaken. First, ref-  
 251 erence values of  $\bar{z}_r$  and of  $\bar{\rho}_r$  are determined. Secondly, a strategy for estimating both  
 252  $z_c$  and  $\bar{\rho}_c$  is developed and applied.

253 Global mean thickness of oceanic crust,  $\bar{z}_r$ , is determined by compiling and analy-  
 254 zing 278 velocity-depth profiles (Figure 7a). These profiles are obtained from modern  
 255 (i.e., waveform-modeled) seismic wide-angle experiments. Our global compilation em-  
 256 braces the existing compilations of White et al. (1992) and Christeson et al. (2019) and  
 257 is tabulated in Supporting Information. Figure 7a indicates that some regions have been  
 258 more intensively studied than others. To mitigate against spatial bias, crustal thickness  
 259 measurements from individual profiles are averaged within  $2^\circ$  bins, which yields a sam-  
 260 ple size of 136. We obtain  $\bar{z}_r = 6.38 \pm 1.12$  km (Figure 7b). In previous studies, Hoggard  
 261 et al. (2016) and Hoggard et al. (2017) used a global mean crustal thickness of  $7.1 \pm 0.8$  km,  
 262 which was gauged from the smaller database of 54 velocity-depth profiles compiled by  
 263 White et al. (1992).

264 The bulk velocity of oceanic crust,  $\bar{v}_p$ , is then used to constrain crustal density. Fig-  
 265 ure 7c shows that  $\bar{v}_p$  varies as a function of crustal thickness. This relationship arises  
 266 from a small but systematic compositional change, which is caused by variations in the  
 267 degree of asthenospheric partial melting at the mid-oceanic ridge where oceanic crust  
 268 is generated (Christensen & Salisbury, 1975; Christensen, 1978). At locations where as-  
 269 thenosphere beneath a mid-oceanic ridge is anomalously hot, the melt fraction is greater,  
 270 which yields thicker crust. Since the depth of isentropic melting is also greater, thicker  
 271 crust is more olivine-rich and so it has a concomitantly higher value of  $\bar{v}_p$ . Note that a  
 272 bulk-velocity assumption is reasonable since porosity does not significantly reduce once

the age of oceanic crust exceeds  $\sim 30$  Ma (Carlson & Herrick, 1990). Empirical studies of core samples and borehole logging records show that crustal velocity,  $v_p$ , and density,  $\rho_c$ , are related such that  $\rho_c = (3.81 \pm 0.02) - (6.0 \pm 0.1)/v_p$  (Carlson and Herrick (1990); Figure 7d). In this way, an empirical relationship between crustal thickness and bulk density can be obtained (Figure 7e). If  $\bar{z}_r = 6.38$  km,  $\bar{\rho}_r = 2.84 \pm 0.07$  Mg m $^{-3}$ .

A revised crustal correction is presented in Figure 8. In contrast to Hoggard et al. (2016) and to Hoggard et al. (2017), who assume that  $\bar{\rho}_c = 2.86 \pm 0.03$  Mg m $^{-3}$ , bulk density is now permitted to vary as a function of crustal thickness (Figure 8a and b). A direct consequence of revising the global mean oceanic thickness and implementing a variable bulk density is that the crustal correction is slightly greater for  $t_c \leq 3$  s or  $z_c \leq 9$  km. The correction is smaller if crustal thickness lies outside of this range of values (Figure 8c and d). In practise, this revised scheme only has a modest effect upon our results. As before, a *Monte Carlo* method is exploited to propagate uncertainties. An uncertainty envelope for the crustal correction is constructed by randomly and repeatedly sampling each parameter value from a Gaussian distribution that is based upon the mean and standard deviation of that parameter (Table 1). In this way, uncertainties in densities of mantle, water and crust, as well as in the velocities of oceanic crust for the two-way travel time case, are incorporated into the crustal correction.

If the Moho discontinuity is clearly visible in either velocity models of seismic wide-angle experiments or on seismic reflection profiles, it is straightforward to use measurements of either  $z_c$  or  $t_c$  to implement crustal corrections. Our global compilation of velocity-depth profiles show that this correction is typically small ( $\pm 0.2$  km). It is important to note that the Moho is not always visible on multi-channel seismic reflection profiles and almost never visible on vintage single-channel seismic reflection profiles. In these instances, crustal thickness is gauged to be either thicker or thinner than the mean global crustal thickness,  $\bar{z}_c$ , on the basis of neighboring crustal thickness measurements. This approach was used by Hoggard et al. (2016) to obtain lower or upper bounds of water-loaded depth to basement. Here, we have formalized this strategy by building a global map of oceanic crustal thickness variation, which delineates regions where crust is either thicker or thinner than the mean value. Figure 9a shows the distribution of high quality controlled-source seismic experiments that include modern waveform-modeled seismic wide-angle experiments and depth-converted seismic reflection profiles. A small number of vintage slope-intercept experiments are also included in locations where modern constraints are unavailable. The results of these slope-intercept experiments are uplifted by 6% to account for the well-known systematic underprediction of crustal thickness (White et al., 1992). This correction ensures that the mean oceanic crustal thickness obtained from vintage slope-intercept modeling matches the mean oceanic crustal thickness obtained from modern experiments. Figure 9b shows how the global distribution of crustal thickness measurements can be used to delineate oceanic regions with crust that is thicker or thinner than  $\bar{z}_r$ . This global extrapolation is especially useful in poorly explored oceanic regions where only vintage single-channel reflection profiles are usually available (Figure 9c).

### 3.3 Revised Plate Model

In order to measure residual depth anomalies, it is first necessary to isolate and remove the dominating influence of plate cooling (Menard, 1973). Oceanic lithosphere cools and subsides as a function of its age (Parsons & Sclater, 1977). In Figure 10a, we present a revised and significantly augmented database of 10,874 age-depth measurements based upon the plate chronology of Seton et al. (2020). These global measurements have been binned every  $1^\circ$ . In terms of plate age, they range from zero age out to 200 Ma and clearly demonstrate the general form that the age-depth relationship takes. At mid-oceanic ridges, water-loaded subsidence is  $2.95 \pm 0.3$  km. Between zero age and  $\sim 60$  Ma, water-loaded subsidence rapidly increases. At greater plate ages, this value tends toward  $\sim 6$  km. The scatter of this cloud of age-depth measurements is  $\pm 1$  km, regardless of plate age.

325 Plate subsidence is generally matched by a decrease in basal heat flow. In Figure 10b,  
 326 we show filtered and binned results of a global compilation of 23,428 heat flow measure-  
 327 ments (Hasterok et al., 2011). This comprehensive database has been corrected, filtered  
 328 and binned using the strategy outlined by F. D. Richards et al. (2018). This strategy  
 329 includes two significant corrections. First, any measurements where the effects of hydrother-  
 330 mal circulation are thought to significantly affect heat flow (i.e., where sediment is thin-  
 331 ner than 0.4 km and within 60 km of seamounts) are removed. Secondly, depression of  
 332 the geothermal gradient when rapid deposition has occurred is taken into account us-  
 333 ing a sedimentation correction (Von Herzen & Uyeda, 1963). The final database of 3,753  
 334 corrected measurements are assigned plate ages from Seton et al. (2020) before being binned  
 335 into windows of 2.5 Ma.

336 Age-depth and heat flow measurements are fitted jointly using a methodology de-  
 337 scribed by F. D. Richards et al. (2018). Their plate model is based upon that originally  
 338 described by Parsons and Sclater (1977) whereby the temperature along the basal bound-  
 339 ary is fixed to simulate resupply of heat (D. P. McKenzie, 1967). F. D. Richards et al.  
 340 (2018) use a more physically reasonable parameterization of thermal conductivity, ther-  
 341 mal expansivity and heat capacity, which builds upon schemes described by D. McKen-  
 342 zie et al. (2005) and by Grose and Afonso (2013).

343 An optimal plate model is presented in Figure 10. This model was obtained by min-  
 344 imizing the combined misfit between observed and calculated age-depth and heat flow  
 345 measurements. The global minimum was identified by carrying out a three-parameter  
 346 sweep: mantle potential temperature,  $T_p$ , is varied between 1100 and 1600°C at inter-  
 347 vals of 25°C; plate thickness,  $z_p$ , is varied between 60 and 160 km at intervals of 5 km;  
 348 and the depth of the ridge axis,  $z_{rd}$ , is varied between 2 and 3 km at intervals of 0.05 km.  
 349 Figure 10c shows that a global minimum misfit of  $\chi_t = 0.19$  is located at  $T_p = 1326 \pm$   
 350  $50^\circ\text{C}$ ,  $z_p = 111 \pm 10$  km and  $z_{rd} = 2.92 \pm 0.5$  km. Uncertainties are gauged from the  
 351  $\chi_t = 0.25$  contour. These recovered values are comparable to independent observational  
 352 constraints. For example, the value of  $T_p$  is consistent with petrologic and geochemical  
 353 estimates (e.g., 1250–1350°C: Katsura et al. (2004); 1280–1400°C: Herzberg et al. (2007);  
 354  $1350 \pm 50^\circ\text{C}$ : Lee et al. (2009); 1314–1464°C: Dalton et al. (2014);  $1318^{+44}_{-32}$  °C: Matthews  
 355 et al. (2016)). The value of  $z_p$  is consistent with the results of stacked surface wave to-  
 356 mographic models which demonstrate that age-dependent shear wave velocity anom-  
 357 lies peter out below about 150 km (e.g., Priestley and McKenzie (2013)).

358 Residual depth anomalies are obtained by measuring vertical distances between ob-  
 359 served age-depth estimates and an optimal plate model. In Figure 11, we compare resid-  
 360 ual depth anomalies calculated using two different plate models. The first model was cal-  
 361 culated by F. D. Richards et al. (2018), who fitted 2,028 age-depth measurements taken  
 362 from Hoggard et al. (2017), using  $T_p = 1300 \pm 50^\circ\text{C}$ ,  $z_p = 135 \pm 30$  km and  $z_{rd} =$   
 363  $2.6 \pm 0.3$  km. When this model is used to construct residual depth anomalies, a minor  
 364 amount of systematic skewness as a function of plate age is discernible (Figure 11b). Neg-  
 365 ative skewness occurs for plate ages of  $\leq 80$  Ma and positive skewness occurs for plate  
 366 ages of  $\geq 80$  Ma.

367 Skewness of residual depth measurements is caused by two inter-related factors. First,  
 368 the revised and augmented database suggests that the age-depth trend has a slightly dif-  
 369 ferent form (i.e., slightly greater subsidence at young ages and slightly smaller subsidence  
 370 at older ages) compared with those age-depth measurements used to generate the plate  
 371 model of F. D. Richards et al. (2018). Secondly, Hoggard et al. (2017) and previous con-  
 372 tributions assume that the solid grain velocity used in the sedimentary correction,  $v_{sg} =$   
 373  $5.5 \text{ km s}^{-1}$ . Here, we adopt a more physically realistic (i.e., less sandy and more silty)  
 374 value of  $v_{sg} = 4.5 \pm 0.5 \text{ km s}^{-1}$ . This reduction means that the sedimentary correc-  
 375 tion for thicker sequences is smaller. Since thicker sequences typically occur on older oceanic  
 376 crust, a smaller correction will contribute toward positive skewness at older ages. Both  
 377 negative and positive skewness are mitigated by refitting the plate model (Figure 11c).

378 Frequency distributions of different subsets of revised residual depth anomalies are sum-  
 379 marized in Figure 11d–f. Both the sediment- and crust-corrected as well as only sediment-  
 380 corrected distributions have similar means and standard deviations with minimal skew-  
 381 ness. Residual depth anomalies generally fall within  $\pm 1$  km regardless of plate age with  
 382 a mean value of  $0.03 \pm 0.49$  km.

383 Finally, it is important to emphasize that both the amplitude and the distribution  
 384 of residual depth anomalies are largely insensitive to specific plate models. This asser-  
 385 tion was carefully and comprehensively tested by Hoggard et al. (2017) who demonstrated  
 386 that alternative plate models such as those described by Parsons and Sclater (1977), Stein  
 387 and Stein (1992) and Crosby et al. (2006) yield global distributions of residual depth anoma-  
 388 lies that are spectrally identical. Hoggard et al. (2017) also showed that similar results  
 389 are obtained even if the physically implausible half-space cooling model is employed, al-  
 390 though this model does not accurately fit a combination of age-depth and heat flow databases  
 391 and, critically, yields a value of  $T_p$  which is unrealistically cool.

### 392 3.4 Geoid Correction

393 The geoid correction,  $C_g$ , ensures that residual depth anomalies are measured with  
 394 respect to a non-hydrostatic equipotential surface (Figure 4a). When identifying key in-  
 395 terfaces on seismic profiles, measurements are calculated relative to sea level. However,  
 396 sea level varies laterally by tens of meters due to density contrasts within the mantle (M. A. Richards  
 397 & Hager, 1984; Hager et al., 1985). This correction is calculated using the Chambat et  
 398 al. (2010) geoid grid. Its size is modest with an rms amplitude of  $\sim 50$  m.

## 399 4 Continental Residual Topography

400 The main reasons for tackling the more difficult problem of continental dynamic  
 401 topography are twofold. First, development of a robust and continuous global represen-  
 402 tation of dynamic topography measurements requires uniformity of coverage. Secondly,  
 403 analysis of continental dynamic topography and associated stratigraphic sequences en-  
 404 ables both spatial and temporal constraints to be obtained. Here, we estimate continen-  
 405 tal residual topography measurements from a range of controlled-source and earthquake  
 406 seismic methods (see S. Stephenson et al. (2021)). The resultant continental database  
 407 comprises 21,739 continental seismic experiments, which include 111 deep seismic reflec-  
 408 tion surveys, 3,037 modern wide-angle experiments, 31 vintage refraction experiments  
 409 and 18,560 receiver function analyses, 16,065 of which exploit the H- $\kappa$  stacking method  
 410 and 2,495 of which have been modeled to provide velocity as a function of depth (Fig-  
 411 ure 1b). Locations and sources of these profiles and experiments, which yield local es-  
 412 timates of crustal thickness and density, are documented in the Supporting Information.

413 A straightforward method for calculating residual topography anomalies is sum-  
 414 marized in Figure 4b. At wavelengths that exceed flexural support, thickness and den-  
 415 sity of continental crust give rise to isostatically compensated topography. This dom-  
 416 inant component of topography is corrected for in order to isolate residual topography,  
 417 which is attributable to a combination of plate thickness changes, asthenospheric tem-  
 418 perature variations and mantle flow. Note that this method differs from that of Hoggard  
 419 et al. (2017), who estimated continental dynamic topography by scaling long wavelength  
 420 (i.e.,  $> 700$  km) free-air gravity anomalies with a constant value of admittance,  $Z = 50$  mGal km $^{-1}$ .

421 The air-loaded continental crustal correction,  $C_{cc}$ , is directly analogous to the oceanic  
 422 crustal correction. Its value adjusts topographic height to allow for the fact that locally  
 423 measured continental crustal thickness and average density,  $z_{cc}$  and  $\bar{\rho}_{cc}$ , both differ from  
 424 the mean global continental crustal thickness and average density,  $\bar{z}_{cr}$  and  $\bar{\rho}_{cr}$ . By iso-  
 425 statically balancing, we obtain

$$C_{cc} = \left( \frac{\rho_a - \bar{\rho}_{cr}}{\rho_a} \right) \bar{z}_{cr} - \left( \frac{\rho_a - \bar{\rho}_{cc}}{\rho_a} \right) z_{cc}. \quad (11)$$

426 Sufficiently accurate values of  $C_{cc}$  are obtained in two steps. First, reference val-  
 427 ues of  $\bar{z}_{cr}$  and  $\bar{\rho}_{cr}$  are determined. An average reference crustal thickness of  $\bar{z}_{cr} = 32.35$  km  
 428 and an average reference crustal density of  $\bar{\rho}_{cr} = 2.78$  Mg m<sup>-3</sup> are obtained from all  
 429 locations within the continental database, which occur at elevations of less than 50 m  
 430 with respect to mean sea level. Secondly, a method for estimating both  $z_{cc}$  and  $\bar{\rho}_{cc}$  has  
 431 been developed and applied (see S. Stephenson et al. (2021)). Values of  $z_{cc}$  are obtained  
 432 from a database of seismically constrained crustal thicknesses (see Supporting Informa-  
 433 tion). Values of  $\bar{\rho}_{cc}$ , which can vary from location to location, are calculated by exploit-  
 434 ing an empirical relationship between acoustic velocity and pressure (Stierman et al., 1979).  
 435 Here, we combine this pressure dependence of seismic velocity with the linear relation-  
 436 ship between density and seismic velocity determined by Ji et al. (2010), which permits  
 437 conversion of a given crustal velocity profile into density. The crustal correction is ap-  
 438 plied to observed topography at each location,  $t_o$ , to isolate the residual topography,  $t_r$ ,  
 439 where  $t_r = t_o + C_{cc} + C_g$ . In order to mitigate the effects of flexural rigidity, observed  
 440 topography is filtered to exclude wavelengths shorter than 50 km.

## 441 5 Results

442 In Figure 12a, we present a revised and augmented map of global residual depth  
 443 anomalies throughout the oceanic realm and of residual topographic anomalies across  
 444 most, but not all, continents. This map builds upon the previous approach developed  
 445 by Hoggard et al. (2016) who focused upon exploiting modern high quality seismic re-  
 446 flection imagery (Figure 12b). We have two goals. First, we want to improve the spa-  
 447 tial resolution of residual depth anomaly measurements throughout the oceanic realm.  
 448 Secondly, we wish to initiate a broadly equivalent analysis on the continents. In both  
 449 cases, any given residual measurement represents the upper limit of observable dynamic  
 450 topography since local variations of lithospheric thickness, that are as yet not accurately  
 451 resolvable, have been neglected.

452 On the continents, spatial coverage is excellent for North America, Eurasia and Aus-  
 453 tralia. It is poorer for South America and Africa. Note that we have deliberately excluded  
 454 measurements from regions dominated by orogenesis and by flexural bending of plates  
 455 (Figure 12c). Both of these processes also act to perturb basement depth but these ef-  
 456 fects are more difficult to isolate and remove with sufficient accuracy. Sources of litho-  
 457 spheric flexure include mountain ranges (e.g. Himalayas, Andes), loading by volcanic seamounts  
 458 (e.g. Hawaiian-Emperor seamount chain), and trenches associated with subduction zones  
 459 (e.g. Peru-Chile trench, Marianas trench). In the oceanic realm, regions directly affected  
 460 by flexure are easily identifiable using a combination of bathymetric maps and seismic  
 461 reflection profiles (Watts & Zhong, 2000; Watts, 2001). On the continents, flexural ef-  
 462 fects were identified using short wavelength free-air gravity anomalies and geologic maps.  
 463 The conservative exclusion polygons shown in Figure 12c are designed to omit continen-  
 464 tal regions dominated by orogenesis. Finally, we have not included residual topographic  
 465 estimates for ice-dominated Antarctica and Greenland.

466 In regions where residual topography measurements are sparse or even absent, the  
 467 distribution and elevation of marine sedimentary rocks are used to constrain positive resid-  
 468 ual topography (Figure 1a). Residual topography,  $t_r$ , is calculated from  $t_r = E + B_p -$   
 469  $SL_p$ , where  $E$  is the present-day height of *bona fide* marine strata,  $B_p$  is water depth at  
 470 time of deposition and  $SL_p$  is sea level at time of deposition. Ages of marine outcrops  
 471 are assigned using biostratigraphic constraints. The most significant uncertainties con-  
 472 cern the values of  $B_p$  and  $SL_p$ . To ensure that estimates of  $t_r$  are maxima, we assume  
 473 that  $SL_p = 0$ . We have also not corrected for water depth at time of deposition which

474 is generally small. Residual topography is calculated with respect to age of marine in-  
 475 undation, which implicitly assumes that there was negligible residual topography when  
 476 strata were originally deposited.

477 Stratigraphic estimates of residual topography are especially useful for Africa, Ara-  
 478 bia and Borneo where there is a lack of well-resolved crustal thickness and density mea-  
 479 surements (O'Malley et al., 2021). Late Cretaceous and Cenozoic marine sedimentary  
 480 rocks are present throughout North Africa and Arabia (Sahagian, 1988). These emer-  
 481 gent strata indicate the extent of the Trans-Saharan Seaway (Petters, 1978; Reymont &  
 482 Dingle, 1987; Benmansour et al., 2016; Luger, 2003). For example, in the Atlas Moun-  
 483 tains along the rim of North Africa, Late Cretaceous limestones are elevated by  $\sim 970$  m  
 484 at the edge of the Kem Kem plateau (Martill et al., 2011). These fine-grained rocks have  
 485 assemblages of definitively marine fish such as actinopterygii (e.g. *Belonostomus sp.*) and  
 486 macrosemyidae (e.g. *Agoultichthys chattertoni*). In northeastern Mali, an interbedded se-  
 487 quence of Eocene carbonate-rich rocks, shales and coarse-grained phosphatic intervals  
 488 are elevated by  $\sim 400$  m (Tapanila et al., 2008). In addition, species of Nigerophiidae  
 489 and Palaeophiidae are reported by McCartney et al. (2018), while (Berggren, 1974) re-  
 490 port a range of echinoderms, cephalopods and benthic foraminifera, which include *Op-*  
 491 *erculinooides bermudezi* and *Cibicides reinholdi* (Berggren, 1974). Along the southern edge  
 492 of the Arabian peninsula, Al-Subbary et al. (1998) document that the shallow marine  
 493 sandstone of the Zijan Member is elevated by more than 2 km, and comprises *Thalassi-*  
 494 *noides* and *Orbitulina discordea*. In Borneo, Oligocene-Neogene marine carbonate rocks  
 495 are used to infer 150 m of post-depositional residual topography (Roberts et al., 2018;  
 496 M. E. Wilson et al., 1999). These carbonate rocks range from 55–5 Ma and formed in  
 497 shallow marine conditions, as indicated by the presence of coralline algae, radiolaria as  
 498 well as foraminifera (Roberts et al., 2018; M. E. Wilson et al., 1999).

499 In summary, observed dynamic topography is constructed using 10,874 residual depth  
 500 measurements from the oceans and 3,777 residual topographic measurements from the  
 501 continents that are averaged into  $1^\circ$  bins. In the oceanic realm, significant positive anoma-  
 502 lies of 1–2 km are linked with the Icelandic, Hawaiian and Afar plumes. There is also  
 503 a substantial long wavelength positive anomaly in the western Pacific Ocean. Significant  
 504 negative anomalies occur in the Argentine abyssal plain, between Australia and Antarc-  
 505 tica, and in the Gulf of Mexico. These long wavelength residual anomalies cannot be sup-  
 506 ported by lithospheric flexure and instead are generated and maintained by mantle con-  
 507 vective processes.

508 On the continents, the spatial pattern of residual topographic measurements is con-  
 509 sistent with observations from the marine realm and with previous onshore studies. For  
 510 example, western North America is dominated by a long wavelength positive residual to-  
 511 pographic anomaly whose existence is corroborated by earthquake tomographic mod-  
 512 els, by the distribution and elevation of marine sedimentary rocks, and by the depth and  
 513 degree of decompression melting determined by geochemical modeling of major, trace  
 514 and rare earth element analyses of basaltic rocks (Klöcking et al., 2018). The edge of the  
 515 eastern seaboard of North America is characterized by small positive anomalies. Pos-  
 516 itive residual topographic anomalies for Madagascar, Spain, Anatolia, India and Borneo  
 517 are similarly consistent with a wealth of independent geologic observations (see, e.g., S. N. Stephen-  
 518 son et al. (2021); Conway-Jones et al. (2019); McNab et al. (2018); Roberts et al. (2018)).  
 519 In Africa and Arabia, a substantial positive anomaly characterizes the Red Sea and the  
 520 adjacent continental margins (J. W. P. Wilson et al., 2014). This anomaly continues down  
 521 through the Afar region into the East African Rift. In South America, positive anoma-  
 522 lies occur along the eastern seaboard from the Borborema region and southward along  
 523 the Serra do Mar escarpment into Patagonia (Rodríguez Tribaldos et al., 2017). Neg-  
 524 ative anomalies dominate the equatorial region. This onshore pattern is consistent with  
 525 adjacent oceanic residual depth measurements. Finally, portions of the eastern seaboard

526 of Australia and the Yilgarn/Pilbara cratons are characterized by positive anomalies (Czarnota  
527 et al., 2014).

## 528 6 Spherical Harmonic Representation

529 The combined oceanic and continental database of residual depth and residual to-  
530 pographic measurements are used to generate a global spherical harmonic representa-  
531 tion of observed dynamic topography. Figure 13 presents a sequence of spherical har-  
532 monic expansions which exploit two complementary methods where the goal is to achieve  
533 smooth and damped representations of unevenly distributed measurements. Method 1  
534 refers to the regularized least-squares inverse algorithm described and applied by Hoggard  
535 et al. (2016). Method 2 refers to an algorithm developed by Valentine and Davies (2020),  
536 which is based upon the statistical theory of Gaussian processes. This approach exploits  
537 an alternative framework for obtaining continuous functions from discrete and noisy mea-  
538 surements that sidesteps perceived difficulties associated with any given basis function  
539 expansion scheme (Rasmussen & Williams, 2006).

540 Here, we have used both of these approaches to build smooth representations out  
541 to maximum spherical harmonic degrees of  $l = 30$  and  $l = 40$ , which correspond to  
542 wavelengths of  $\sim 1300$  km and  $\sim 1000$  km, respectively. Since our revised and augmented  
543 database is both more evenly sampled and no longer small, the results of applying these  
544 two different methods are strikingly similar both for  $l = 30$  (compare Figure 13a and  
545 d) and for  $l = 40$  (compare Figure 13b and e). Similarities between these different rep-  
546 resentations can be objectively assessed by measuring the difference between recovered  
547 amplitudes (Figure 13g and h). It is evident that there is little significant difference at  
548 either  $l = 30$  or  $l = 40$  for densely sampled portions of the oceanic and continental  
549 realms. We note that any marked differences are confined to Antarctica and Greenland,  
550 where we have not included any residual topographic measurements, and to orogenic belts,  
551 such as the Himalayas, which have been omitted. Inclusion of elevation measurements  
552 of uplifted marine strata across North Africa, Arabia and Borneo help to stabilize spher-  
553 ical harmonic representations in these regions. Figure 13c and f present the  $l = 1-3$  com-  
554 ponents of both  $l = 40$  representations, which are almost identical—rms amplitudes are  
555 0.20 km and 0.18 km, respectively. Both recovered planforms of observed dynamic to-  
556 pography are strikingly similar with peak long wavelength amplitudes of  $\pm 0.5$  km. Fig-  
557 ure 13i confirms that the difference between these low degree representations is negligible—  
558 represented values from each grid are within  $\pm 0.2$  km of each other at almost any given  
559 location.

560 Hoggard et al. (2016) fitted spherical harmonic functions to their global database  
561 up to, and including,  $l = 30$  which yielded a residual misfit of  $\chi^2 \sim 1$ . The results nec-  
562 essarily imply that shorter wavelength functions are required to adequately fit the ob-  
563 servational database. Here, we contend that higher degree structure up to, and includ-  
564 ing,  $l = 40$  is recoverable from our revised and augmented database, which achieves an  
565 enhanced sampling density. Hoggard et al. (2017) used a *Monte Carlo* cross-validation  
566 scheme to formally demonstrate the presence of higher degree structure. They corrob-  
567 orated their conclusions by visually comparing individual spot measurements and dif-  
568 ferent spherical harmonic representations along two transects which we re-analyze here  
569 (Figure 14 and Figure 15). Along both the West African and North Pacific transects,  
570 we demonstrate improved fits between spot measurements and spherical harmonic rep-  
571 resentations out to at least  $l = 30$  and, probably,  $l = 40$ . Similar results are obtained  
572 for each transect regardless of which spherical expansion method is used. The 8,000 km  
573 transect along oceanic lithosphere adjacent to the West African coastline confirms the  
574 existence of a series of dynamic topography swells with amplitudes of  $\sim 1$  km and wave-  
575 lengths of  $\sim 1000$  km (Figure 14). Positive residual depth anomalies are associated with  
576 volcanic rocks of the Cameroon Line (+700 m), with the Angolan Dome (+1000 m) and  
577 with the Namibian Dome (+700 m). Negative residual depth anomalies are associated

578 with the Niger Delta (−500 m) and with the Congo Delta (−400 m). The 12,000 km tran-  
 579 sect from the North Pacific Ocean reveals residual depth anomalies associated with the  
 580 Hawaiian Swell (+1200 m) together with Magellan Seamounts and the Marshall-Gilbert  
 581 Seamounts (Figure 15).

582 Independent geologic and geophysical validation of any spherical harmonic repre-  
 583 sentation of observed dynamic topography is of considerable importance. Here, we high-  
 584 light two significant tests (Figure 16). The first test concerns the spatial relationship be-  
 585 tween the distribution of Neogene-Quaternary intraplate basaltic rocks and positive resid-  
 586 ual depth anomalies (Ball et al. (2021); Figure 16a). Visual correlation between these  
 587 two different databases demonstrates that there is a striking co-location of youthful in-  
 588 traplate magmatism and positive dynamic topography. This co-location is corroborated  
 589 by global surface wave topographic models which indicate that the distribution of intraplate  
 590 magmatism also correlates with sub-plate negative shear wave velocity anomalies and  
 591 with thin lithosphere (Ball et al., 2021). The second test concerns the relationship be-  
 592 tween long wavelength dynamic topography and the geoid (Hager & Richards, 1989). Fig-  
 593 ure 16b presents the longest wavelength component (i.e.  $l = 1-3$ ) of our spherical har-  
 594 monic representation. It shows that the maximum amplitude at these longest wavelengths  
 595 is less than  $\pm 500$  m which disagrees with many, but not all, predicted models of dynamic  
 596 topography. Significantly, the planforms of observed long wavelength dynamic topogra-  
 597 phy and of the geoid are in broad agreement.

## 598 7 Discussion

599 Power spectral analysis of observed dynamic topography has been undertaken for  
 600 several related reasons. First, we wish to assess differences between spherical harmonic  
 601 representations obtained using alternative methodologies described by Hoggard et al. (2016)  
 602 and by Valentine and Davies (2020). Secondly, we are interested in testing the stabil-  
 603 ity of these power spectra when they are extended out to higher spherical harmonic de-  
 604 grees. Thirdly, we want to assess the spatial limits of spherical harmonic representation  
 605 in terms of maximum achievable degree (i.e. minimum wavelength). Finally, we consider  
 606 the physical meaning of recovered power spectra from the perspective of mantle flow mod-  
 607 eling.

608 Figure 17a presents two power spectra obtained using the regularized least-squares  
 609 inverse algorithm out to and including spherical harmonic degrees 30 and 40, respectively.  
 610 These spectra are very similar, which suggests that the recovered spectral slope is a stable  
 611 feature. Both spectra are in agreement with the results obtained by Hoggard et al.  
 612 (2016), confirming that the power of observed dynamic topography is a function of  $k^{-1}$   
 613 (i.e. pink noise) where

$$k = \frac{\sqrt{l(l+1)}}{R}. \quad (12)$$

614  $R = 6,371$  km is the radius of the Earth. The limits of spectral recoverability can be as-  
 615 sessed by measuring the reduced chi-squared statistical measure,  $\chi_v^2$ , where

$$\chi_v^2 = \frac{1}{v} \sum_i \frac{(O_i - C_i)^2}{\sigma_i^2}. \quad (13)$$

616  $v$  is the degree of freedom which is determined by the number of observations,  $n$ , minus  
 617 the number of fitted parameters,  $m$ .  $O_i$  and  $C_i$  are observed and calculated values, re-  
 618 spectively, and  $\sigma$  is variance. The value of  $\chi_v^2$  steadily declines from  $\sim 6$  as higher spher-  
 619 ical harmonic degrees are included (Figure 17b and d). Significantly,  $\chi_v^2$  continues to de-  
 620 crease monotonically between  $l = 30$  and  $l = 40$  at which point its value still exceeds  
 621 1. This observation implies that spot measurements have not been overfitted, confirm-

ing what is qualitatively apparent along transects presented in Figures 14 and 15. Figure 17c presents a power spectrum, out to and including  $l = 40$ , obtained using an alternative method for spherical harmonic representation described by Valentine and Davies (2020). This spectrum and the accompanying decrease of  $\chi_v^2$  as a function of  $l$  are practically identical to what is presented in Figure 17a and b. Previously reported differences between the Hoggard et al. (2016) and Valentine and Davies (2020) spectra are evidently caused by a combination of sparse and uneven coverage of spot measurements across the oceanic realm together with an absence of continental control. Analysis of the revised and extensively augmented database presented here has ameliorated these differences. Note that each method yields different uncertainty envelopes since errors are computed in different ways. Hoggard et al. (2016) gauged spectral uncertainty by analyzing a suite of spherical harmonic representations with different gradient regularizations and amplitude damping coefficients. Valentine and Davies (2020) used sampling of the *a posteriori* distribution obtained by computing  $10^5$  randomly generated models where each model is a realization of global residual topography that is compatible with observations, uncertainties and the Bayesian prior. Spectra are computed for each model as a function of spherical harmonic degree. In this way, the median, the interquartile range and the width for each of the central 50% and 99% are estimated.

Spatial limitations of these spherical harmonic representations are determined by two unrelated constraints. The first constraint is the limit beyond which the amplitude of spectral power approaches a putative floor of uncertainty, whose value is determined by measurement error. The fact that  $\chi_v^2$  is greater than 1 at  $l = 40$  suggests that the floor of uncertainty has not quite been reached. Nevertheless, we think that it would be unwise to pursue  $l > 40$  unless observational error can be significantly reduced below  $\pm 100$  m. The second constraint is related to spatial contamination by lithospheric flexure at shorter wavelengths. Flexural wavelength is determined by the elastic thickness of a plate,  $T_e$ . There is considerable debate about the spatial pattern of  $T_e$  and its maximum value. According to Tesauro et al. (2012), the value of  $T_e$  rarely exceeds 100 km and other studies suggest that this value is an upper limit (Watts, 2001). The half-wavelength of flexural support,  $x_b$ , for a line load that is imposed upon a broken plate is given by

$$x_b = \left[ \frac{4\pi^4 E T_e^3}{12g(1 - \sigma^2)(\rho_m - \rho_s)} \right]^{\frac{1}{4}}, \quad (14)$$

where  $E = 70$  GPa is Young's Modulus,  $g = 9.81 \text{ m s}^{-2}$  is gravitational acceleration,  $\sigma = 0.25$  is Poisson's ratio,  $\rho_m = 3.33 \text{ Mg m}^{-3}$  is mantle density, and  $\rho_s$  is the density of infilling material (Gunn, 1943). For air-loaded topography,  $\rho_s = 0 \text{ Mg m}^{-3}$ . If  $T_e = 100$  km,  $x_b = 523$  km and the flexural wavelength is  $2x_b = 1046$  km which corresponds to a spherical harmonic degree of  $l = 38$ . It is reasonable to conclude that spectral analysis out to  $l = 40$  has approached the flexural limit. Beyond this soft limit, flexural effects begin to contaminate power spectra. It is difficult, but not impossible, to isolate residual depth anomalies when flexural bending is significant (Levitt & Sandwell, 1995).

Finally, the shape of the observed power spectrum provides an important constraint about the nature of mantle convection. We exploit a straightforward analytical approach to illuminate the nature of this constraint. If mantle viscosity varies as a function of radius alone, M. A. Richards and Hager (1984) showed that a spectral approach can be used to calculate deflection at the Earth's surface,  $\delta a^{lm}$ , where

$$\delta a^{lm} = \frac{1}{\Delta\rho_a} \int_r^a A^l(r) \delta\rho^{lm}(r) dr. \quad (15)$$

$\Delta\rho_a$  is the density difference between mantle and overlying fluid (i.e., water or air),  $A^l(r)$  are the normalized surface response kernels as a function of radial distance down through the mantle,  $r$ , and  $\delta\rho^{lm}(r)$  represents mantle density anomalies. Superscripts  $l$  and  $m$

668 refer to spherical harmonic degree and order, respectively. The limits of integration are  
 669  $r = 0$  to  $r = a$  where  $a = 2890$  km represents the Earth's surface (Figure 18a). The  
 670 normalized surface response kernels,  $A^l(r)$ , depend upon the radial viscosity structure  
 671 of the mantle (see, e.g., Steinberger et al. (2010)). Mantle density anomalies,  $\delta\rho^{lm}(r)$ ,  
 672 can be estimated from global shear wave tomographic models. In this way, it is possi-  
 673 ble to calculate surface deflection,  $\delta a^{lm}$ , for different viscosity models (M. A. Richards  
 674 & Hager, 1984).

675 Here, we use an analytical model based upon instantaneous Stokes' flow to explore  
 676 the relationship between surface response kernels, density structure and surface deflec-  
 677 tion. Equation 15 is straightforward to solve if we assume that both  $A^l(r)$  and  $\delta\rho^{lm}(r)$   
 678 have simple functional form. First, the normalized surface response kernels are approx-  
 679 imated by

$$A^l(r) = \exp(-kr), \quad (16)$$

680 where  $k = 2\pi/\lambda$  is wavenumber. Representative functions of  $A^l(r)$  are shown in Fig-  
 681 ure 18b. These functions are very similar to those calculated from the radial viscosity  
 682 structure presented by Lambeck et al. (1996). Secondly, the average density anomaly as  
 683 a function of radius is approximated by

$$\delta\rho^{lm}(r) = b(r - c)^2, \quad (17)$$

684 where  $b = 1 \times 10^{-12}$  kg m<sup>-5</sup> determines the size of the average density anomaly  
 685 at any given depth and  $c = 1500$  km ensures that the average density anomaly in the  
 686 middle of the lower mantle is of negligible size. This approximation is shown in Figure  
 687 18d. In this way, Equation 15 can be rewritten as

$$\delta a^{lm} = \frac{1}{\Delta\rho_a} \int_r^a b(r - c)^2 \exp(-kr) dr, \quad (18)$$

688 which, after integration, yields

$$\delta a^{lm} = \frac{1}{\Delta\rho_a} \left[ \frac{bc^2}{k} - \frac{2bc}{k^2} + \frac{2b}{k^3} - \exp(-kr) \left\{ \frac{b(r - c)^2}{k} + \frac{2b(r - c)}{k^2} + \frac{2b}{k^3} \right\} \right]. \quad (19)$$

689 This relationship is used to calculate surface deflection as a function of spherical har-  
 690 monic degree (Figure 18e).

691 It is possible to calculate  $\delta\rho^{lm}(r)$  from earthquake tomographic models by scaling  
 692 shear wave velocity anomalies. The relationship between density and shear wave veloc-  
 693 ity anomalies is given by

$$\frac{\delta\rho}{\rho} = \left( \frac{d \ln \rho}{d \ln V_s} \right) \frac{\delta V_s}{V_s} \quad (20)$$

694 where  $\delta V_s/V_s$  and  $\delta\rho/\rho$  are fractional shear wave velocity and fractional density anoma-  
 695 lies, respectively. (Forte, 2007) shows that the optimal scaling factor is  $d \ln \rho / d \ln V_s \sim$   
 696 0.1. He argues that this factor varies as a function of depth through the mantle (see Fig-  
 697 ure 12a in Forte (2007)). This variation is approximated using

$$\frac{d \ln \rho}{d \ln V_s} = \beta \cos \left( \frac{\pi r}{3000} \right)^2 \quad (21)$$

698 where  $\beta$  is a constant. The best-fitting power spectrum is obtained for  $\beta = 0.06$ .

699 Peak power is at  $l = 2$ , which demonstrates that dynamic topography is domi-  
700 nated by longer wavelength ( $10^4$  km) components, albeit with amplitudes of  $< 500$  m.  
701 Significant power exists out to  $l = 40$ , which indicates that shorter wavelength ( $10^3$  km)  
702 components play an important role, highlighting the influence of shallow mantle density  
703 variations. This fit is predicated upon two important assumptions. First, average radial  
704 density anomalies are implicitly assumed to contribute to surface dynamic topography  
705 for all values of  $k$ . In other words, density distribution within the convecting mantle is  
706 assumed to be spectrally white. Secondly, we require average radial density anomalies  
707 within the upper mantle to be a factor of two smaller than inferred by linearly convert-  
708 ing shear wave velocity anomalies into density anomalies (Forte, 2007). This inference  
709 is supported by a combination of experimental and seismological evidence, which shows  
710 that the relationship between  $V_s$  and  $\rho$  becomes markedly non-linear for asthenospheric  
711 potential temperatures exceeding  $1200^\circ\text{C}$  as a consequence of anelasticity (Yamauchi &  
712 Takei, 2016). A small value of  $\beta$  is in agreement with F. D. Richards et al. (2020), who  
713 matched observed and calculated power spectra by combining density anomalies constructed  
714 from the S40RTS and SL2013sv tomographic models with an anelastic parametrization  
715 (Ritsema et al., 2011; Schaeffer & Lebedev, 2013).

716 In summary, the wider purpose of this discussion is threefold. First, we wish to demon-  
717 strate that the power spectrum of observed dynamic topography can be robustly recover-  
718 ed from a global inventory of residual depth and residual topographic measurements.  
719 The slope of this spectrum does not depend upon the particular method used for spher-  
720 ical harmonic representation. It also does not depend upon whether this representation  
721 is carried out to spherical harmonic degree  $l = 30$  or higher. Secondly, we suggest that  
722 our revised and augmented global inventory of measurements can now be fitted out to  
723 spherical harmonic degree  $l = 40$ , which corresponds to a wavelength of  $\sim 10^3$  km. This  
724 wavelength represents a possible lower bound for mantle convective phenomena, which  
725 has immediate fluid dynamical implications. Finally, we use an analytical approach to  
726 show that the slope of the observed power spectrum is consistent with Stokes' flow as-  
727 sociated with mantle density anomalies.

## 728 8 Conclusions

729 We present a revised and augmented global database of oceanic residual depth mea-  
730 surements ( $n = 10,874$ ). These measurements were constructed by analyzing large in-  
731 ventories of seismic reflection, modern wide-angle and legacy refraction profiles. In gen-  
732 eral, residual depth anomalies have amplitudes of  $\pm 1$  km. They provide a valuable con-  
733 straint for the present-day planform of dynamic topography since they can be used to  
734 benchmark global numerical experiments of mantle flow. This study has yielded a num-  
735 ber of useful ancillary datasets. For example, detailed interpretations of the sediment-  
736 basement interface along more than 7000 seismic reflection profiles provide benchmarks  
737 for global maps of sedimentary thickness variation. A synthesis of crustal thickness mea-  
738 surements from 278 modern wide-angle experiments has yielded a revised average oceanic  
739 crustal thickness of  $6.38 \pm 1.12$  km together with an assessment of oceanic crustal thick-  
740 ness variation. Finally, a global dataset of accurate water-loaded depth to basement mea-  
741 surements enables a revised plate cooling model to be determined, which will help to im-  
742 prove our understanding of the thermal evolution of oceanic lithosphere.

743 We combine these oceanic measurements with continental measurements ( $n = 3,777$ )  
744 to generate spherical harmonic representations of observed dynamic topography using  
745 two different inverse methods. Our results indicate that both of these methods yield closely  
746 similar results on a global basis. This similarity is most apparent when power spectra  
747 are constructed. Spectral analysis of both spherical harmonic representations demon-  
748 strates that dynamic topography features a peak at  $l = 2$  ( $10^4$  km) and maintains con-  
749 siderable power at  $l = 40$  ( $10^3$  km). By making simplifying assumptions about the  
750 surface response kernels and radial density structure of the mantle, an analytical spec-

751 trum is calculated. The slope and power of this spectrum matches observed spectra which  
752 confirms that mantle flow plays a significant role in generating and maintaining dynamic  
753 topography.

754 **9 Open Research**

755 The data described in this study are available on Mendeley Data ([https://data](https://data.mendeley.com/datasets/f79bw527cg/draft?a=6c5f3ebe-c5d1-4b77-9ffb-978ed0c85d97)  
756 [.mendeley.com/datasets/f79bw527cg/draft?a=6c5f3ebe-c5d1-4b77-9ffb-978ed0c85d97](https://data.mendeley.com/datasets/f79bw527cg/draft?a=6c5f3ebe-c5d1-4b77-9ffb-978ed0c85d97)).  
757 Academic single-channel seismic reflection profiles are freely available from [https://www](https://www.marine-geo.org)  
758 [.marine-geo.org](https://www.marine-geo.org). Commercial seismic reflection profiles have previously been presented  
759 by Hoggard et al. (2017) in their Supporting Information. The software packages have  
760 been previously published by Hoggard et al. (2016) and Valentine and Davies (2020). For  
761 access to these software packages please contact those authors.

762 **Acknowledgments**

763 MCH is supported by the Gates Cambridge Trust. We are grateful to D. Al-Attar, I. Frame,  
764 A. Jackson, D. Lyness, R. A. Weissel, C. O'Malley and A. Valentine for their help. De-  
765 partment of Earth Sciences contribution number esc.XXXX.

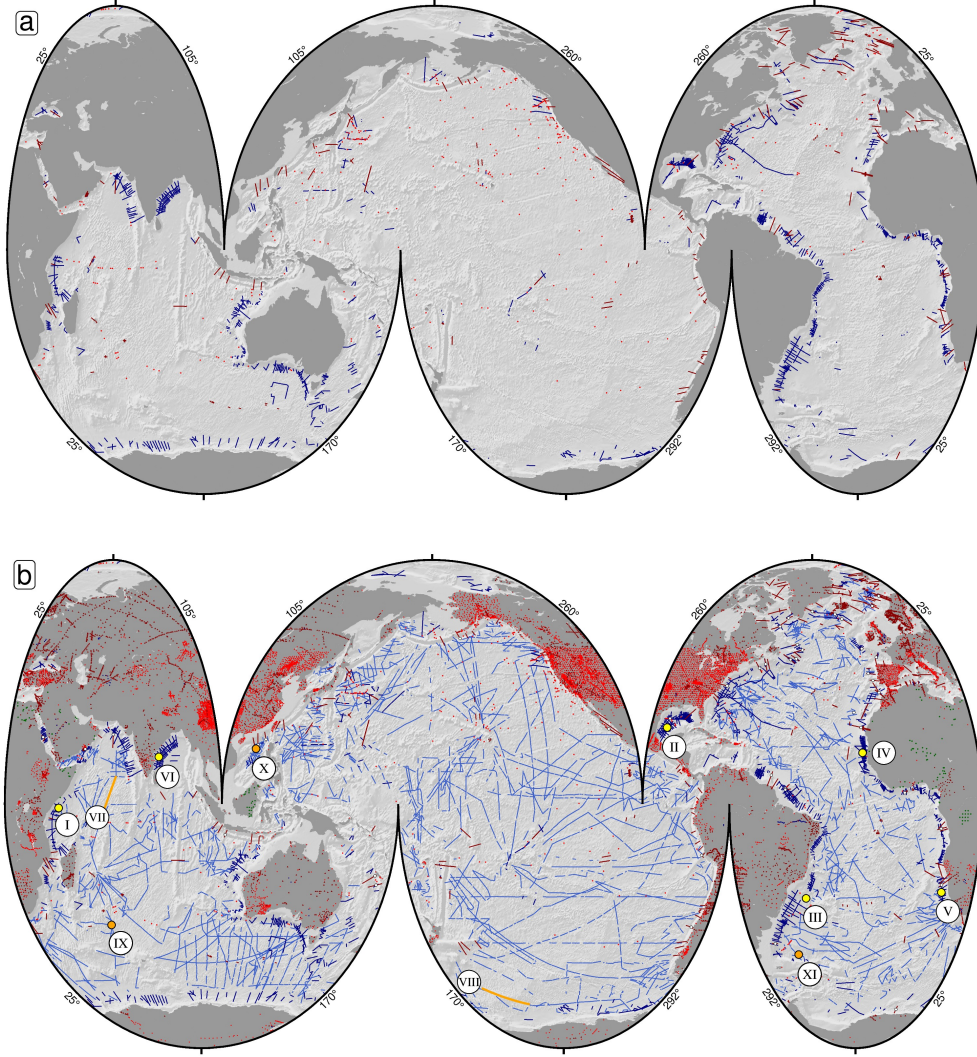


**Figure 1. Maps of seismic databases.** (a) Segmented Mollweide projection of global bathymetry sampled every  $0.25^\circ$ . Oceanic database originally compiled by Hoggard et al. (2017) that includes 1,725 seismic experiments. Dark blue lines = 1,065 multi-channel seismic reflection profiles; dark red lines = 260 waveform-modeled seismic wide-angle experiments; red circles = 400 slope-intercept refraction experiments. (b) Revised and augmented database compiled in this study that includes 7,601 oceanic and 21,739 continental seismic experiments. Dark blue lines = 1,411 multi-channel seismic reflection profiles; light blue lines = 5,444 single-channel seismic reflection profiles; dark blue circles = 111 continental seismic reflection profiles; dark red lines = 323 waveform-modeled seismic wide-angle experiments; dark red circles = 2,495 receiver function experiments which have been modelled; red circles = 423 oceanic slope-intercept refraction experiments and 16,065 continental receiver function experiments for which the H-k stacking method was applied; dark red triangles = 3,037 waveform-modelled wide angle studies (i.e., post-1980); red triangles = 31 vintage refraction (i.e., pre-1980); green circles = 132 marine depositional constraints for selected continental regions; white circles = 43 coincident seismic wide-angle and reflection experiments used to calculate sedimentary correction (Figure 5); yellow circles = locations of modern multi-channel seismic reflection images shown in Figure 2; orange circles/lines = locations of vintage single-channel seismic reflection images shown in Figure 3. Locations and sources of experiments used to compile database are tabulated in Supporting Information.

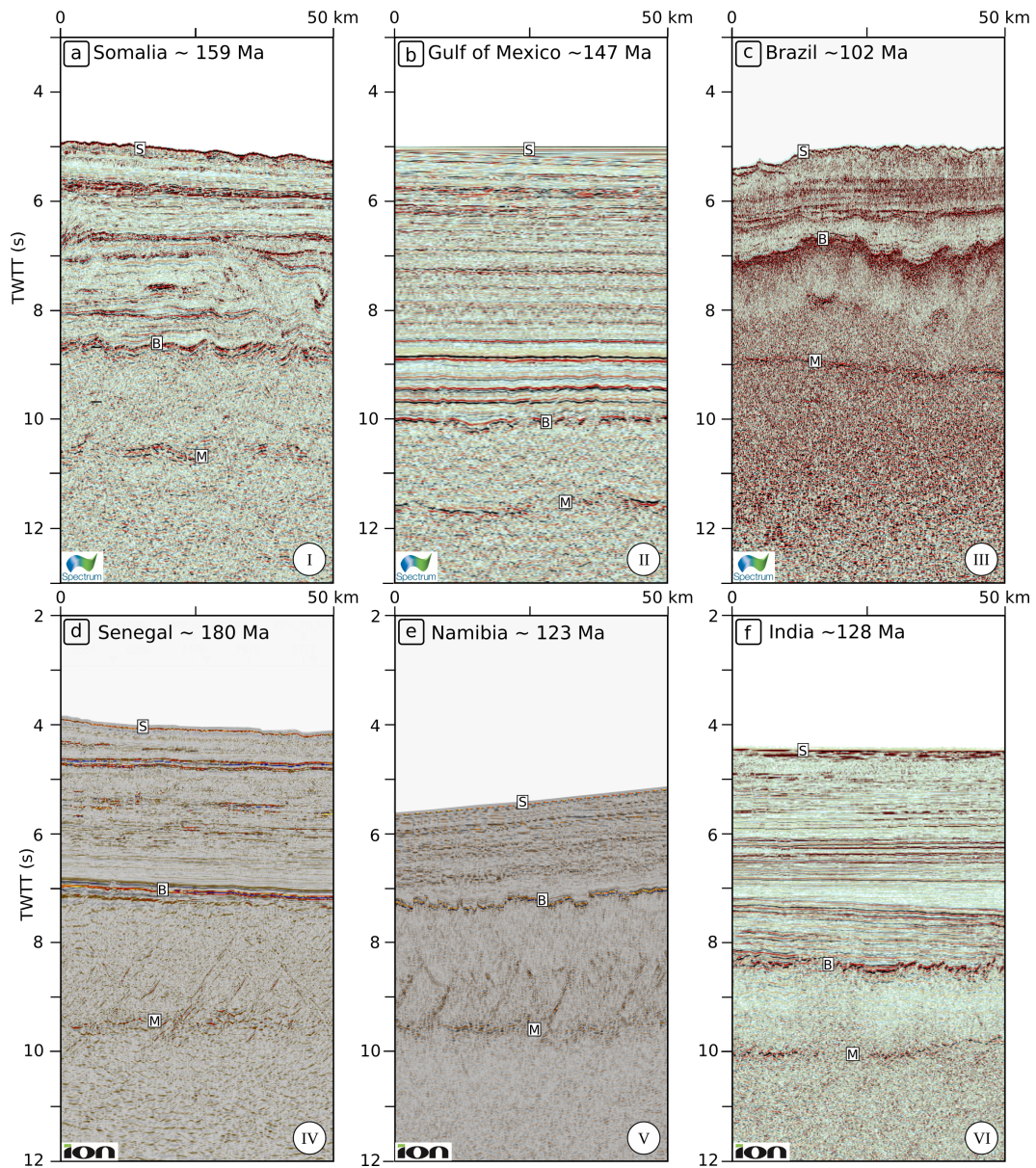


**Figure 2. Modern images of oceanic crust.** (a) Multi-channel seismic reflection profile of 159 Ma oceanic crust from offshore Somalia. S = seabed; B = sediment-basement interface; M = Moho (i.e. base of crust); TWTT = two-way travel time. (b) Gulf of Mexico (147 Ma). (c) Offshore Brazil (102 Ma). (d) Offshore Senegal (180 Ma). (e) Offshore Namibia (123 Ma). (f) Offshore India (128 Ma). Numbered profile locations shown in Figure 1. Crustal ages taken from global age grid (Seton et al., 2020). Images are shown courtesy of ION and Spectrum.

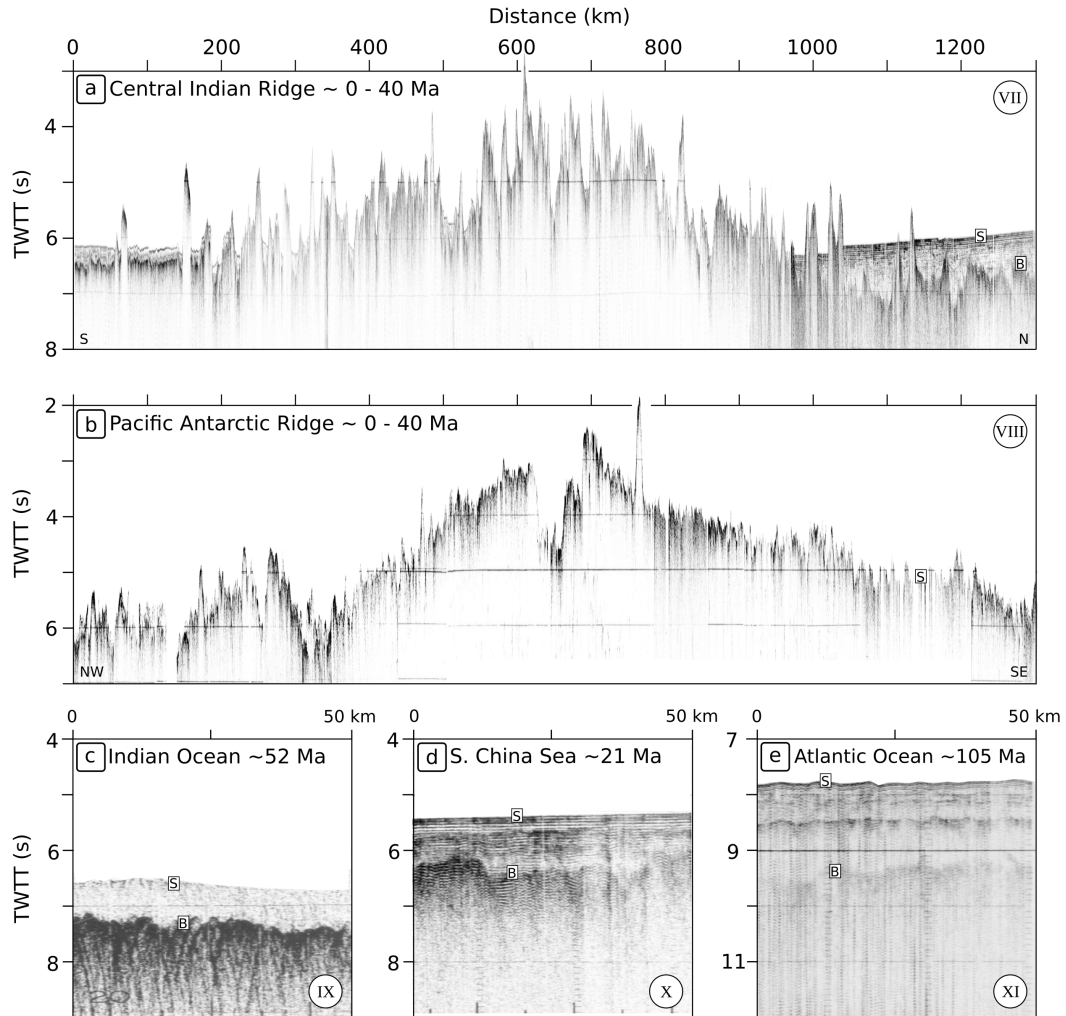


**Figure 3. Vintage images of oceanic crust.** (a) Single-channel seismic reflection profile of 0–40 Ma oceanic crust from central Indian Ridge. S = seabed; B = sediment-basement interface; TWTT = two-way travel time. (b) Pacific-Antarctic Ridge (0–40 Ma). (c) Indian Ocean (52 Ma). (d) South China Sea (21 Ma). (e) South Atlantic Ocean (105 Ma). Numbered profile locations shown in Figure 1. Crustal ages taken from global age grid (Seton et al., 2020). Images taken from Academic Seismic Portal of Lamont-Doherty Earth Observatory (<https://www.marine-geo.org>).

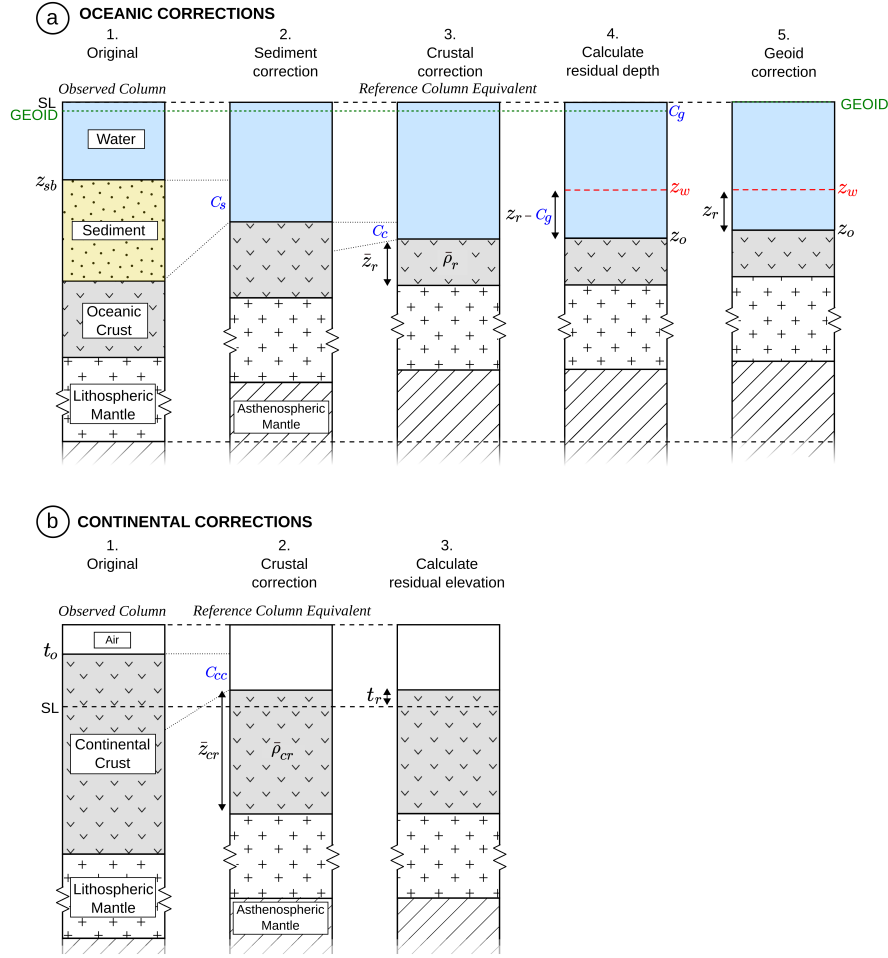


**Figure 4. Sedimentary and crustal corrections.** (a) 1. Observed column of oceanic lithosphere loaded with sediment and water.  $SL$  = mean sea level;  $z_{sb}$  = depth of the seabed. 2. Column where sedimentary layer is converted into equivalent water load referred to as sedimentary correction,  $C_s$ . 3. Reference column where thickness of oceanic crust is converted into mean global thickness,  $\bar{z}_r = 6.38$  km, and mean global density,  $\bar{\rho}_r = 2.84 \text{ Mg m}^{-3}$ , which results in additional water load referred to as crustal correction,  $C_c$ . 4. Column which shows difference between expected depth to oceanic basement of known age,  $z_w$ , and observed depth to basement,  $z_o$  such that  $z_w - z_o = z_r - C_g$  where  $C_g$  is geoid correction. Geoidal reference surface shown by green dashed line. 5. Column which shows residual depth anomaly,  $z_r$ , obtained by applying sedimentary, crustal, age-depth and geoid corrections. Modified from Hoggard et al. (2017). (b) 1. Observed column of continental lithosphere.  $t_o$  = observed topography. 2. Reference column where thickness and density of crust is converted to mean global thickness and density.  $C_{cc}$  = crustal correction;  $\bar{z}_{cr} = 32.35$  km is the mean thickness of continental crust;  $\bar{\rho}_{cr} = 2.78 \text{ Mg m}^{-3}$  is the mean density of continental crust. 3. Column showing residual topographic anomaly,  $t_r$ , obtained by isostatic balance.

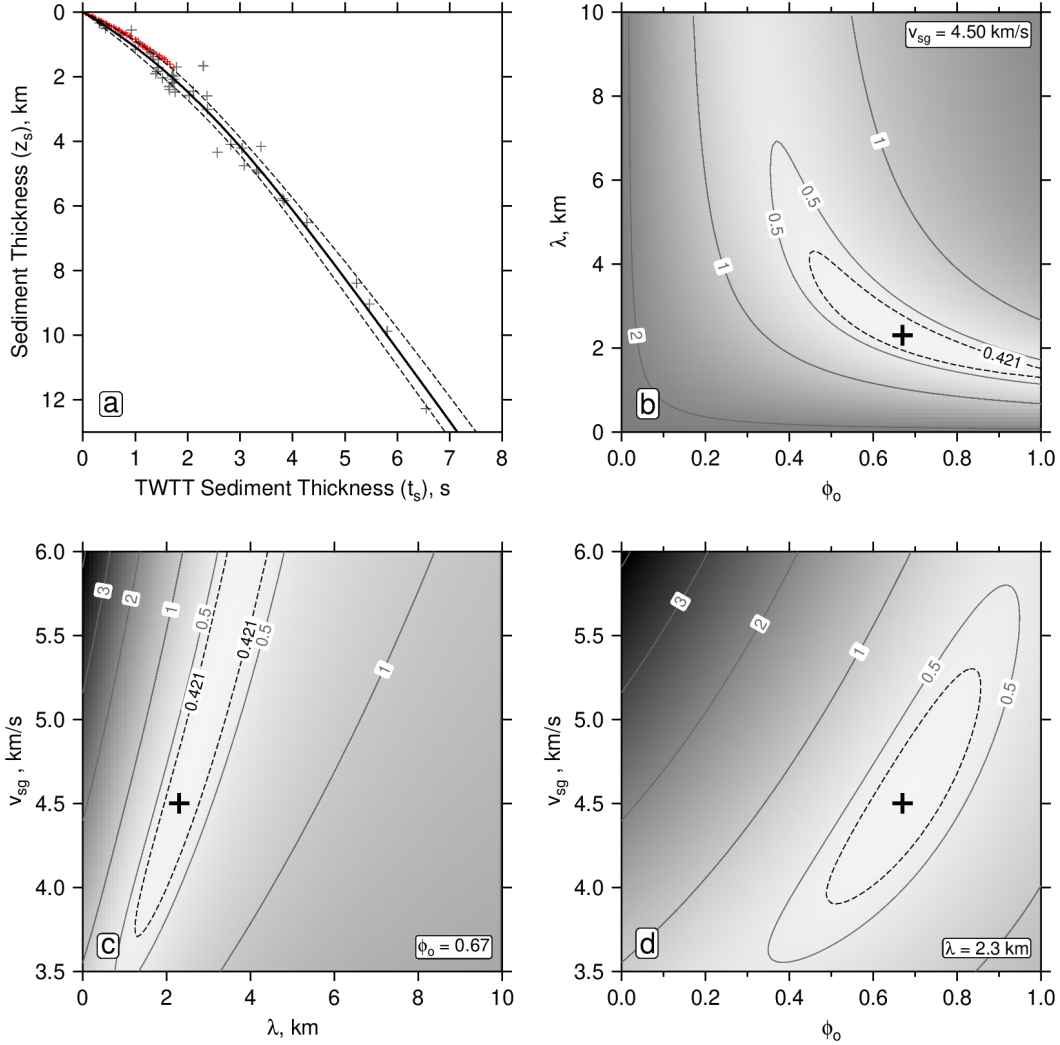


**Figure 5. Sediment velocity and compaction.** (a) Time-depth relationship. Black crosses = 43 TWTT-depth pairs of sedimentary thickness measured from coincident seismic reflection and wide-angle experiments from Hoggard et al. (2017). Solid/dashed lines = best-fit velocity model with one standard deviation (i.e., rms misfit  $\leq 0.421$ ); red crosses = legacy observations from boreholes (Crough, 1983). (b) Misfit plotted as function of  $\phi_0$  and  $\lambda$  for  $v_{sg} = 4.5 \text{ km s}^{-1}$ . Black cross = global minimum at  $\phi_0 = 0.67$  and  $\lambda = 2.3 \text{ km}$ ; dashed contour numbered 0.421 encompasses all  $\phi_0$ - $\lambda$  pairs for  $v_{sg} = 4.5 \text{ km s}^{-1}$  that fit 67% of TWTT-depth pairs. (c) Misfit plotted as function of  $v_{sg}$  and  $\lambda$  for  $\phi_0 = 0.67$ . (d) Misfit plotted as function of  $v_{sg}$  and  $\phi_0$  for  $\lambda = 2.3 \text{ km}$ . Note that value of  $v_{sg}$  is smaller than that assumed by Hoggard et al. (2017).

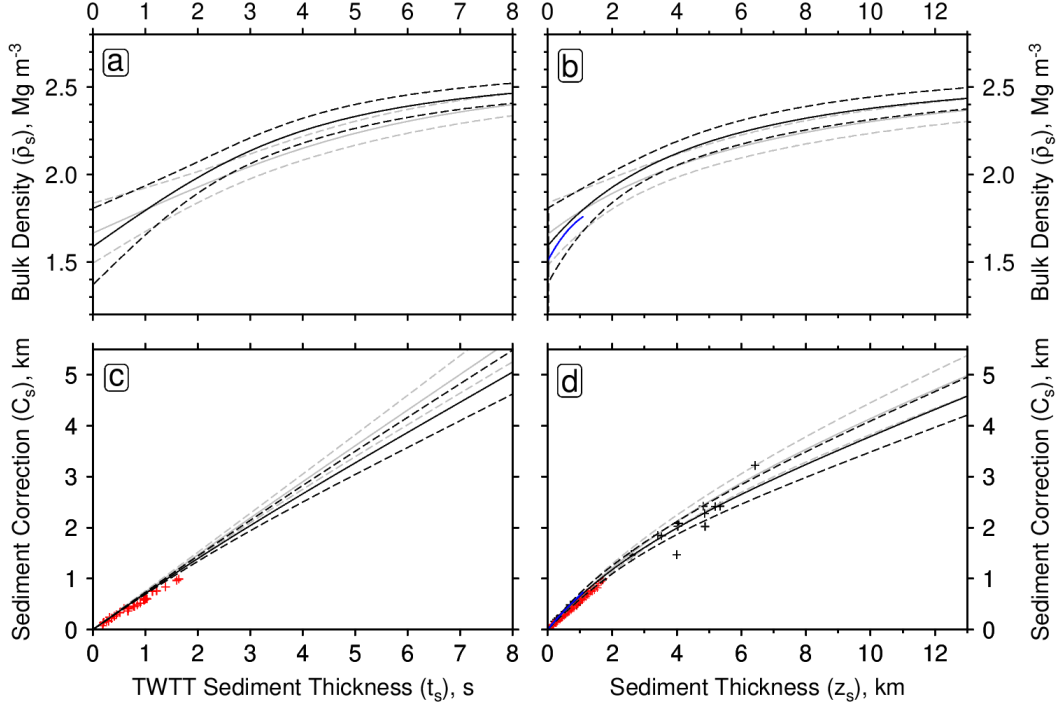


**Figure 6. Sedimentary density and isostatic corrections.** (a) Bulk sedimentary density,  $\bar{\rho}_s$ , plotted as function of TWTT. Black solid/dashed lines = relationship calculated using Equation 9 with standard deviation arising from uncertainties in compaction parameters, velocities, and densities of water and solid grains (Table 1); gray solid/dashed lines = relationship used by Hoggard et al. (2017). (b) Same plotted as function of sediment thickness where standard deviation arises from compaction parameters and densities alone. Blue line = bulk sediment density variation estimated from 1263 oceanic drilling sites (Rowley, 2019). (c) Sedimentary correction plotted as function of TWTT. Black solid/dashed lines = relationship calculated using Equation 3 where standard deviation includes uncertainties in all input parameters (Table 1); Gray solid/dashed lines = relationship used by Hoggard et al. (2017); red crosses = sedimentary corrections of Crough (1983); (d) Same plotted as function of sediment thickness. Blue line = relationship used by Rowley (2019); red crosses = corrections of Crough (1983); black crosses = corrections of Louden et al. (2004) and of Sykes (1996) based upon down-hole logs and seismic wide-angle surveys.

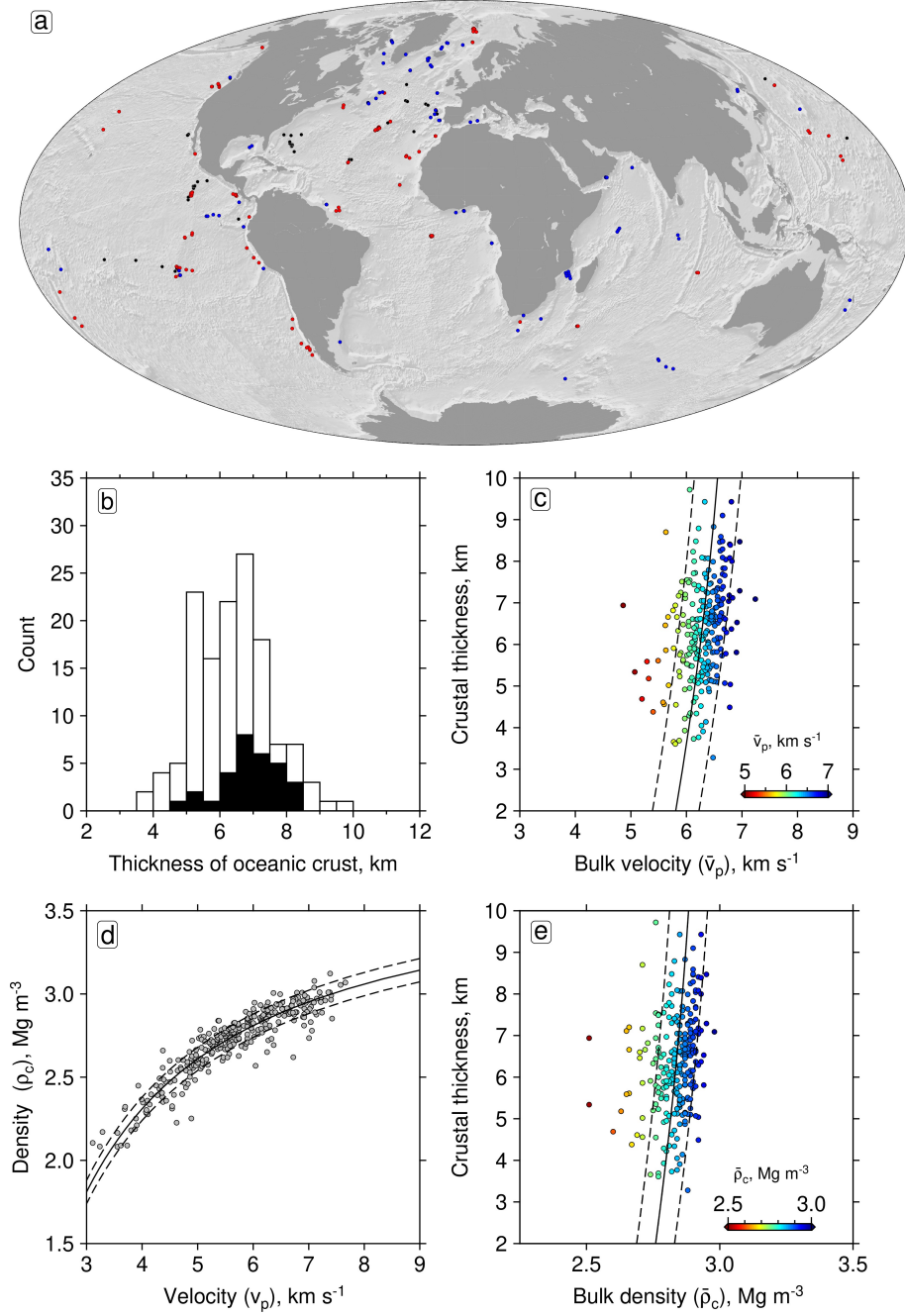


**Figure 7. Oceanic crustal measurements** (a) Loci of 278 crustal velocity profiles. Black circles =  $v_p$  profiles compiled by White et al. (1992); red circles =  $v_p$  profiles compiled by Christeson et al. (2019); blue circles = additional  $v_p$  profiles compiled for this study (see Supporting Information). Shaded bathymetry calculated from ETOPO1 model (Amante & Eakins, 2009). (b) Open histogram = crustal thickness estimates for 278 profiles averaged within 2° bins where crust  $\leq 10$  km (mean crustal thickness =  $6.38 \pm 1.12$  km for  $n = 136$ ); black histogram = crustal thickness estimates for 54 profiles compiled by White et al. (1992) averaged within 2° bins (mean crustal thickness =  $6.90 \pm 0.82$  km for  $n = 30$ ). (c) Crustal thickness plotted as function of bulk  $v_p$  for 278 profiles averaged within 2° bins. Circles are colored according to bulk  $v_p$ ; solid/dashed lines = mean/standard deviation. (d) Relationship between density of oceanic crustal rocks and  $v_p$  (Carlson & Herrick, 1990). Gray circles = laboratory measurements; solid/dashed line = mean/standard deviation. (e) Crustal thickness plotted as function of calculated bulk density. Circles are colored according to bulk density; solid/dashed line = mean/standard deviation. Note that in panels (b) and (d), empirical relationships for  $\bar{v}_p$  and  $\bar{\rho}_c$  have also been extrapolated to oceanic crust thickness of 20 km.

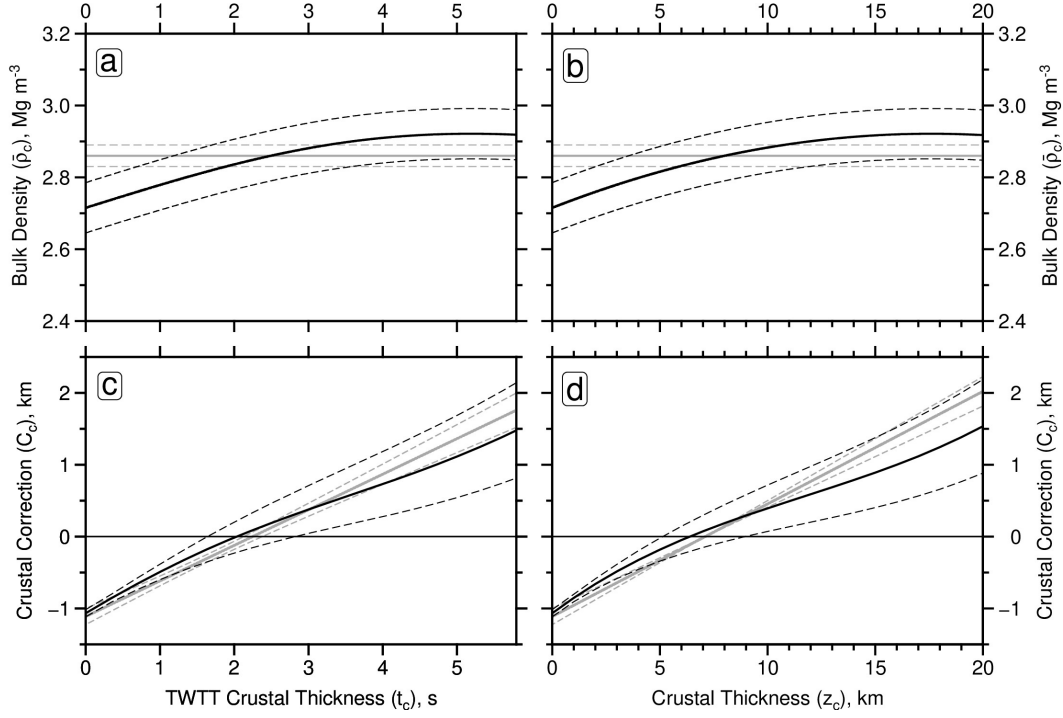


**Figure 8. Crustal density and isostatic corrections.** (a) Bulk density plotted as function of crustal thickness in TWTT. Black solid/dashed lines = relationship calculated using information presented in Figure 7 with standard deviation arising from uncertainties in velocity and density measurements (Carlson & Herrick, 1990); gray solid/dashed lines = constant value of density and its uncertainty assumed by Hoggard et al. (2017). (b) Same plotted as function of crustal thickness in km. (c) Crustal correction,  $C_c$ , plotted as function of crustal thickness in TWTT. Black solid/dashed lines = relationship and standard deviation calculated using information presented in Figure 7; gray solid/dashed lines = relationship calculated by Hoggard et al. (2017). (d) Same plotted as function of crustal thickness in km.

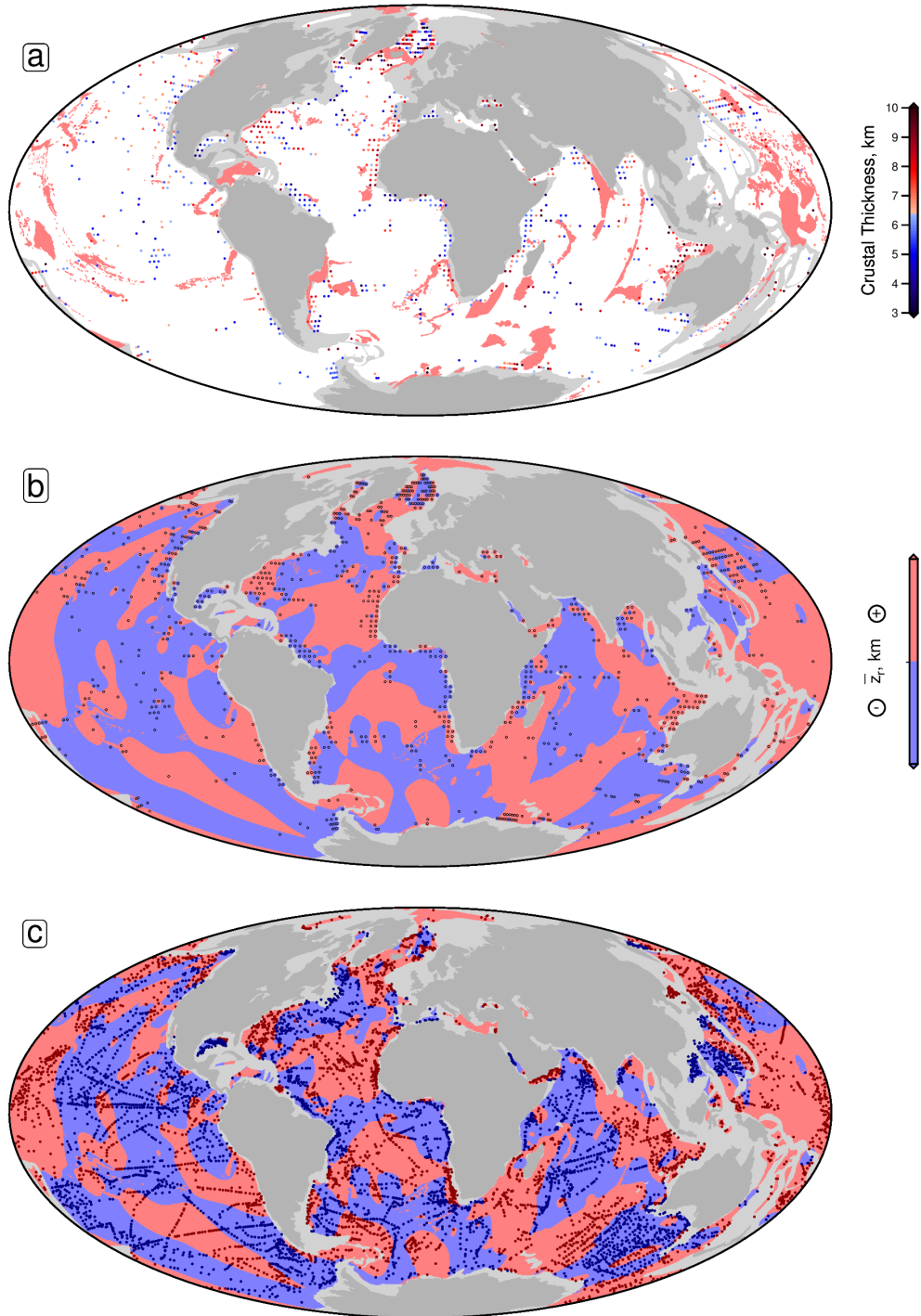


**Figure 9. Crustal thickness interpolation.** (a) Global distribution of oceanic crustal thickness measurements from 384 waveform-modeled wide-angle seismic experiments, 388 depth-converted seismic reflection profiles, and 250 vintage slope-intercept refraction experiments. Warm/cool colors = measurements which are thicker/thinner than mean oceanic crustal thickness,  $\bar{z}_r = 6.38$  km; pink polygons = large igneous provinces associated with anomalously thick oceanic crust (Coffin et al., 2006); gray polygons = extent of continental crust (Seton et al., 2020). (b) Interpolated global distribution of thicker/thinner oceanic crust. Red/blue polygons = crust that is thicker/thinner than mean oceanic crustal thickness; circles = measurements shown in panel (a). (c) Same overlay with oceanic database shown in Figure 1. Red/blue circles = loci of multi-channel and single-channel seismic reflection profiles.

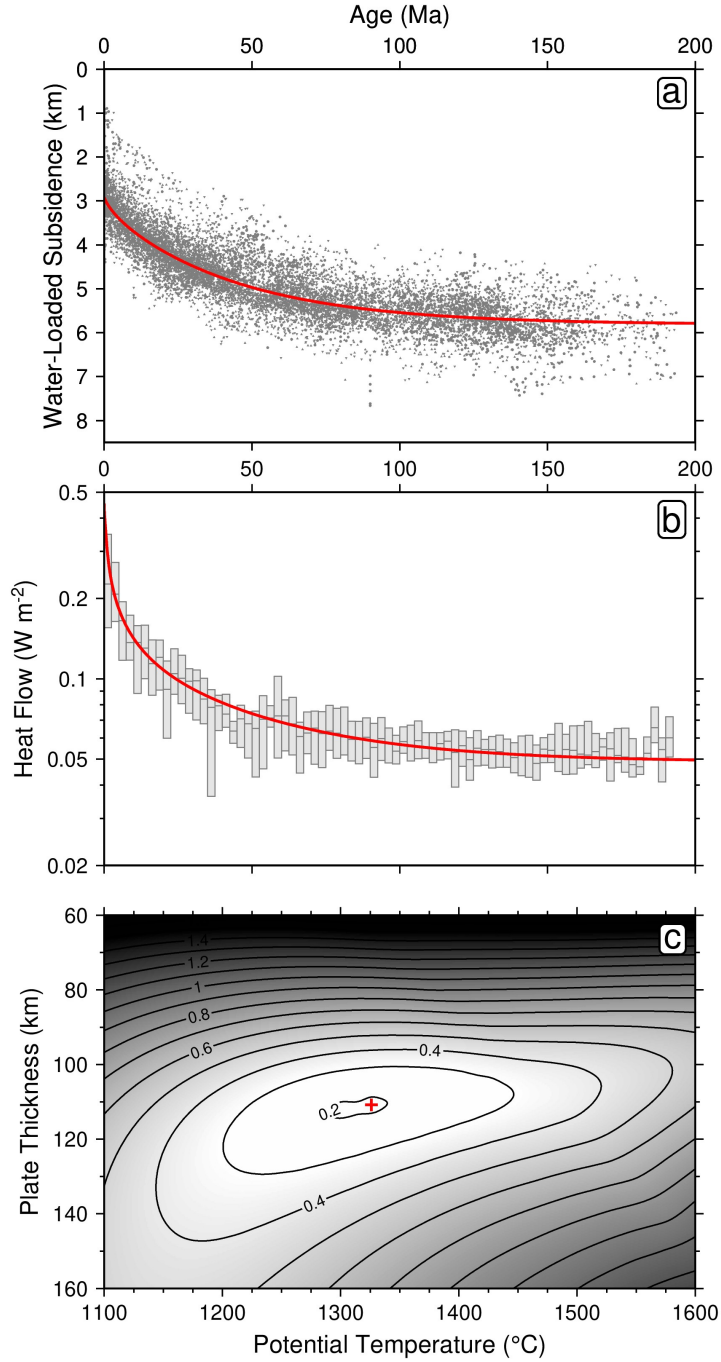


**Figure 10. Plate model.** (a) Revised age-depth inventory. Gray circles = water-loaded depth measurements to oceanic basement averaged within  $1^{\circ}$  bins and plotted as function of plate age; red line = optimal age-depth relationship obtained by jointly fitting water-loaded depth and heat flow measurements. (b) Heat flow plotted as function of plate age. Gray boxes with horizontal bars = interquartile ranges of heat flow measurements with median values; red line = optimal relationship obtained by jointly fitting water-loaded depth measurements and heat flow measurements. (c) Joint misfit,  $\chi_t$ , between observed and calculated subsidence and heat flow observations sliced at best fitting zero-age depth of 2.92 km.

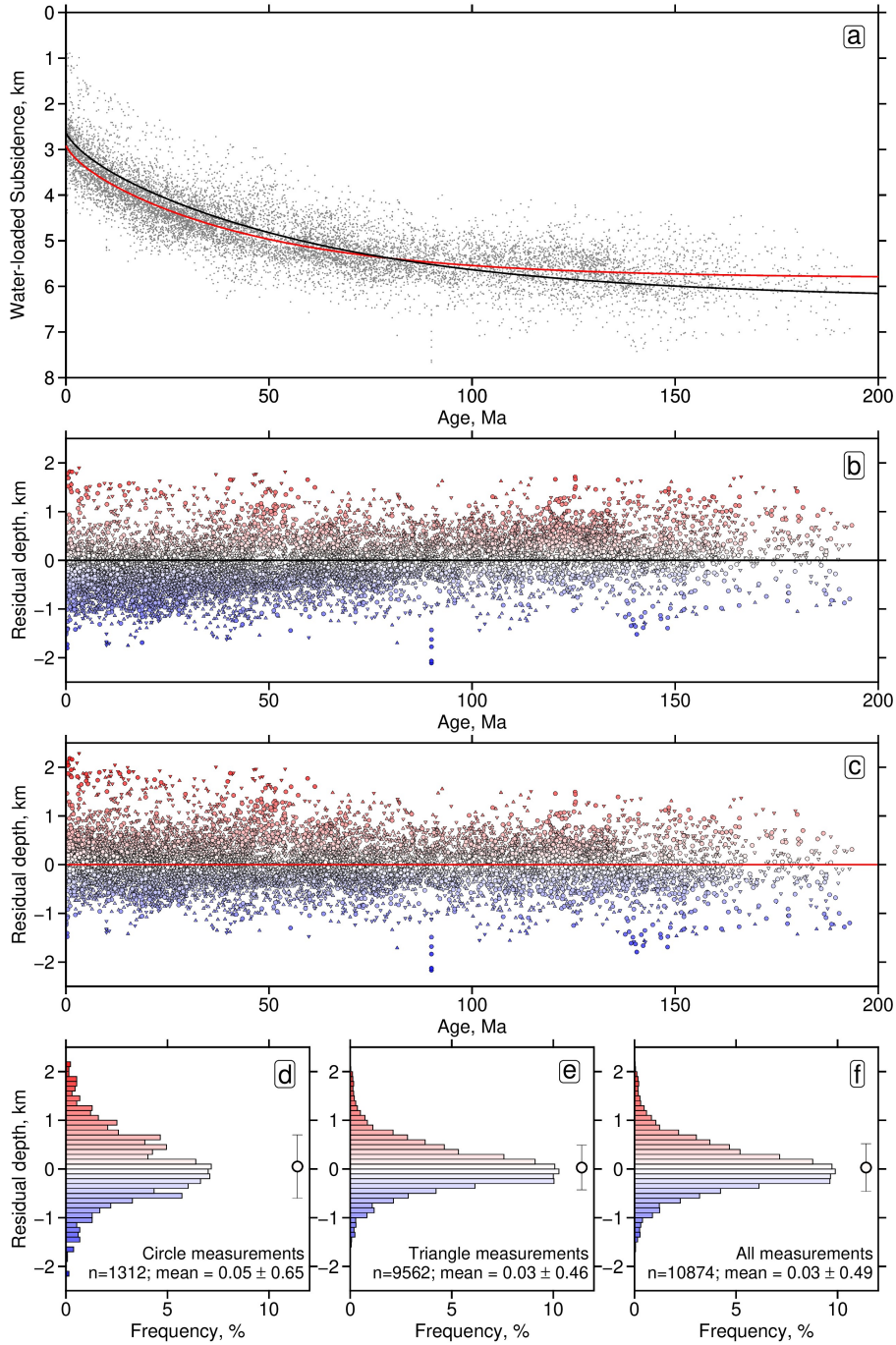


**Figure 11. Global compilation of residual depth spot measurements.** (a) Water-loaded depth to oceanic basement measurements averaged within  $1^\circ$  bins. Red line = revised plate model generated as part of this study (see Figure 10); black line = plate model of F. D. Richards et al. (2018). (b) Residual depth measurements plotted with respect to plate model of F. D. Richards et al. (2018). Red/white/blue points = positive/zero/negative residual depth anomalies; horizontal black line = plate model. Note tilt of measurements between 0 and 200 Ma. (c) Residual depth measurements plotted with respect to revised plate model. Note absence of tilt. (d) Histogram of residual depth measurements where both sediment and crustal corrections have been carried out. (e) Same for measurements where only sediment correction has been applied. (f) Same for all residual depth measurements.

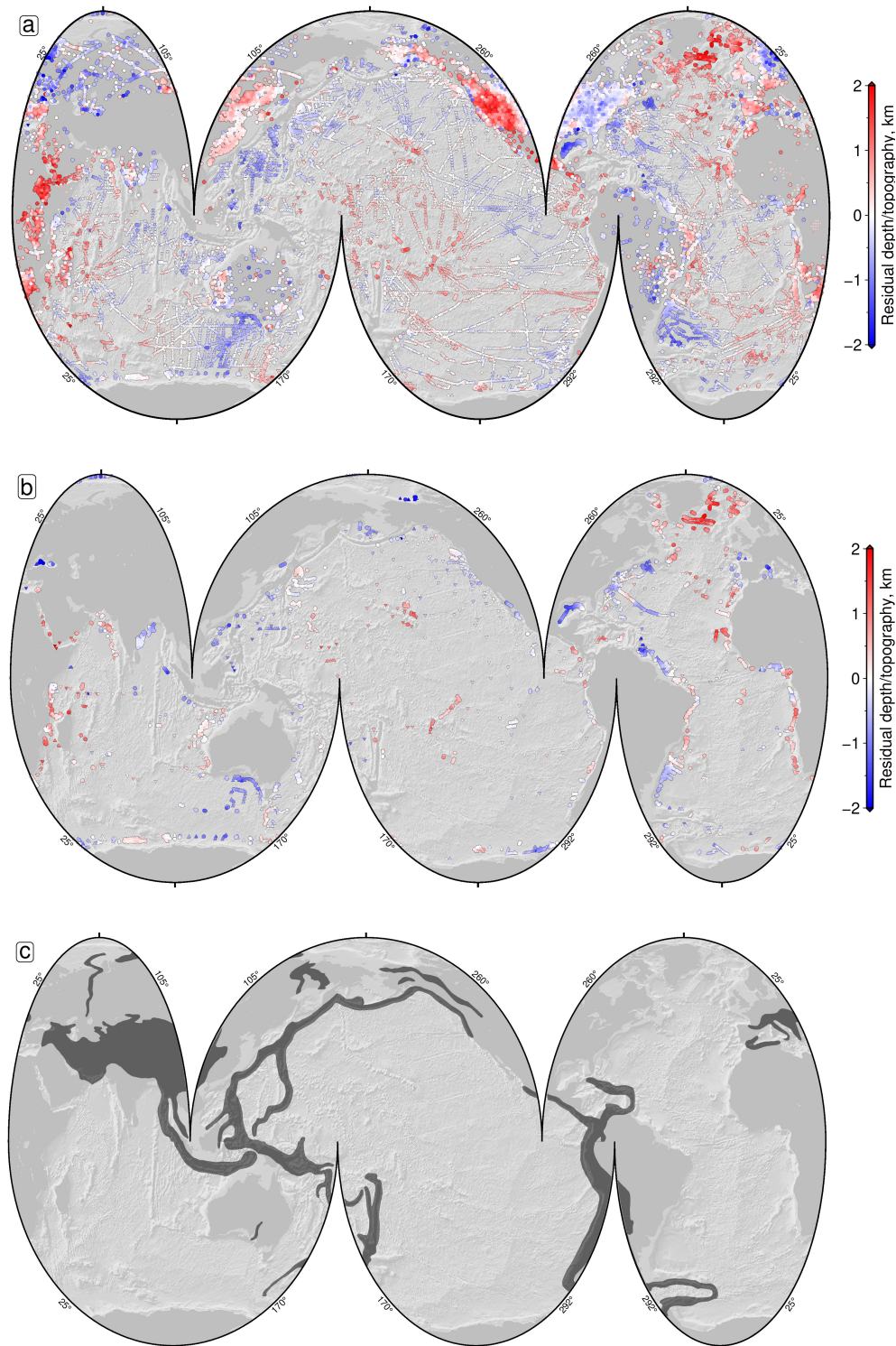


**Figure 12. Global map of residual bathymetry/topography.** (a) 10,874 oceanic residual bathymetric and 3,777 continental residual topographic measurements averaged within  $1^\circ$  bins that were compiled in this study. In oceanic realm, circles = measurements with both sediment and crustal corrections; downward/upward-pointing triangles = measurements that are upper/lower limits with only sedimentary corrections (sign of crustal correction inferred from regional constraints). In continental realm, large circles = measurements obtained by analysis of receiver functions, by controlled source seismic wide-angle and by vintage refraction experiments; small circles = elevations of onshore marine strata. (b) 2,297 oceanic residual bathymetric measurements averaged within  $1^\circ$  bins that were compiled by Hoggard et al. (2017). In oceanic realm, symbols are same as panel (a). (c) gray polygons = excluded regions that include active orogenic belts and zones of flexural bending. See Supporting Information.

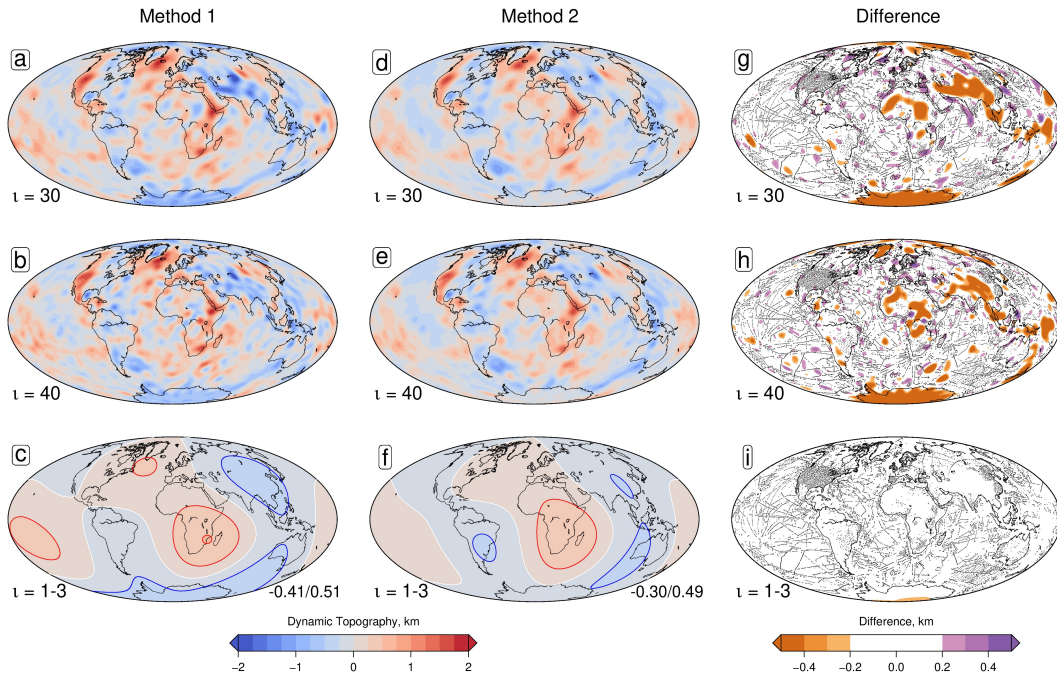


**Figure 13. Spherical harmonic representations of observed dynamic topography.** (a)–(c) Spherical harmonic representations of residual depth measurements at spherical harmonic degree  $l = 30$ ,  $l = 40$  and  $l = 1-3$  of  $l = 40$  representation. Method 1 = regularized least-squares inverse algorithm (Hoggard et al., 2016). Values displayed at lower right-hand side of plot (c) are min/max values of grid. (d)–(f) Same for Method 2 = Gaussian Process algorithm (Valentine & Davies, 2020). (g)–(i) Difference between two methods. Black circles = residual depth/topographic constraints).

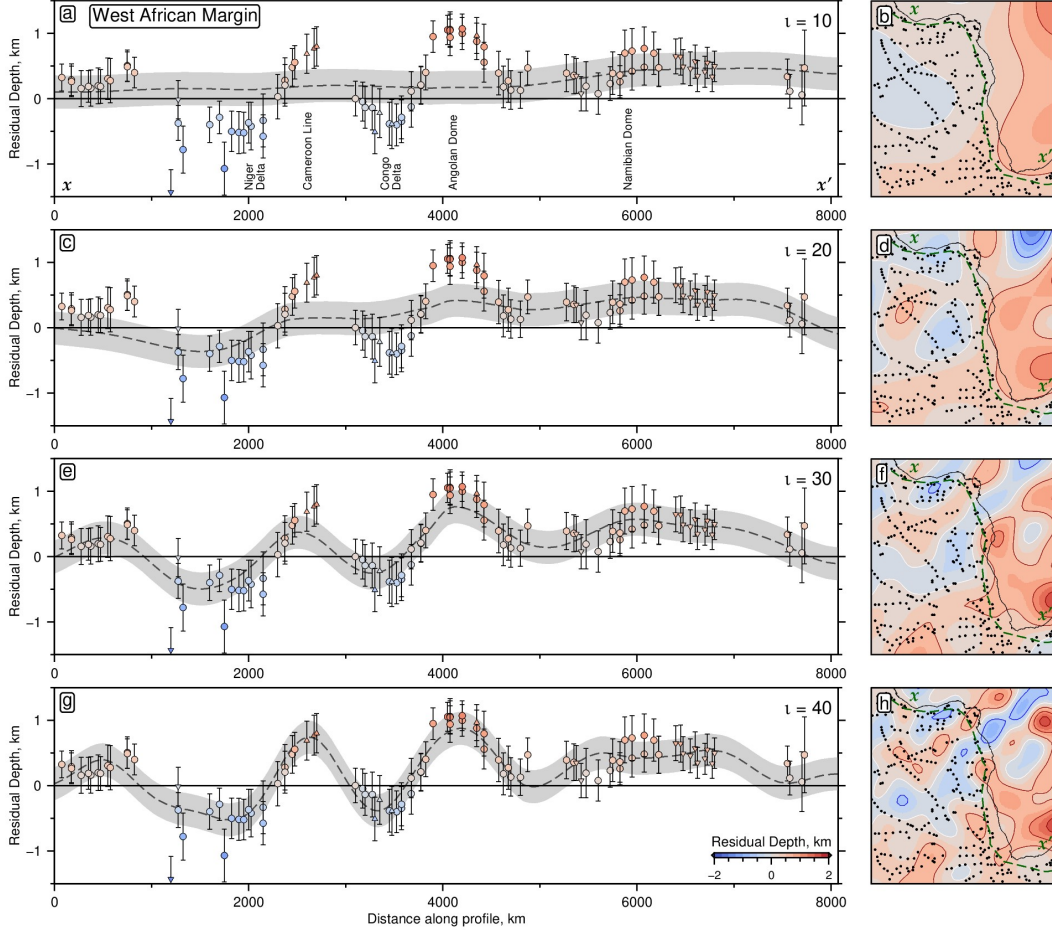


**Figure 14. West African transect.** (a) Residual depth anomaly measurements, averaged within  $1^\circ$  bins, from 80 km wide corridor along oldest oceanic lithosphere adjacent to West African coastline shown in panel (b). Colored circles/triangles with vertical bars = measurements as previously described with  $1\sigma$  uncertainties; dashed line with gray band = spherical harmonic representation using the regularized least-squares inversion algorithm for  $l = 10$  with uncertainty of  $\pm 250$  m. Note that the location of this transect closely approximates that presented by Hoggard et al. (2017). (b) Map of residual depth anomalies. Dashed line = locus of transect shown in panel (a); black dots = residual depth anomaly measurements averaged within  $2^\circ$  bins; contours and color shading = spherical harmonic representation for  $l = 10$  that is contoured every 0.5 km. (c) and (d) same for  $l = 20$ . (e) and (f) same for  $l = 30$ . (g) and (h) same for  $l = 40$ .

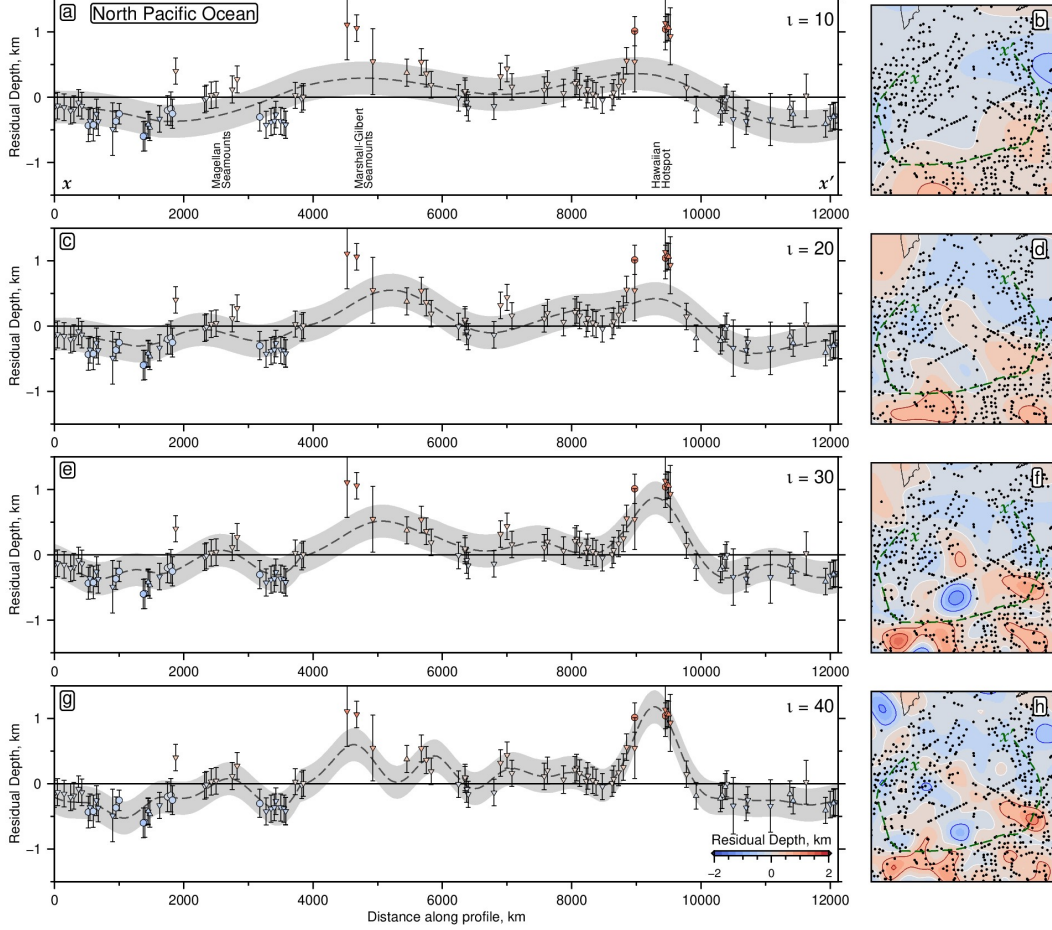


**Figure 15. North Pacific Ocean transect.** (a) Residual depth anomaly measurements, averaged within  $1^\circ$  bins, from 80 km wide corridor along transect shown in panel (b). Colored circles/triangles with vertical bars = measurements as previously described with  $1\sigma$  uncertainties; dashed line with gray band = spherical harmonic representation using the regularized least-squares inversion algorithm for  $l = 10$  with uncertainty of  $\pm 250$  m. Note that the location of this transect is slightly different to that presented by Hoggard et al. (2017). (b) Map of residual depth anomalies. Dashed line = locus of transect shown in panel (a); black dots = residual depth anomaly measurements averaged within  $2^\circ$  bins; contours and color shading = spherical harmonic representation for  $l = 10$  that is contoured every 0.5 km. (c) and (d) same for  $l = 20$ . (e) and (f) same for  $l = 30$ . (g) and (h) same for  $l = 40$ .

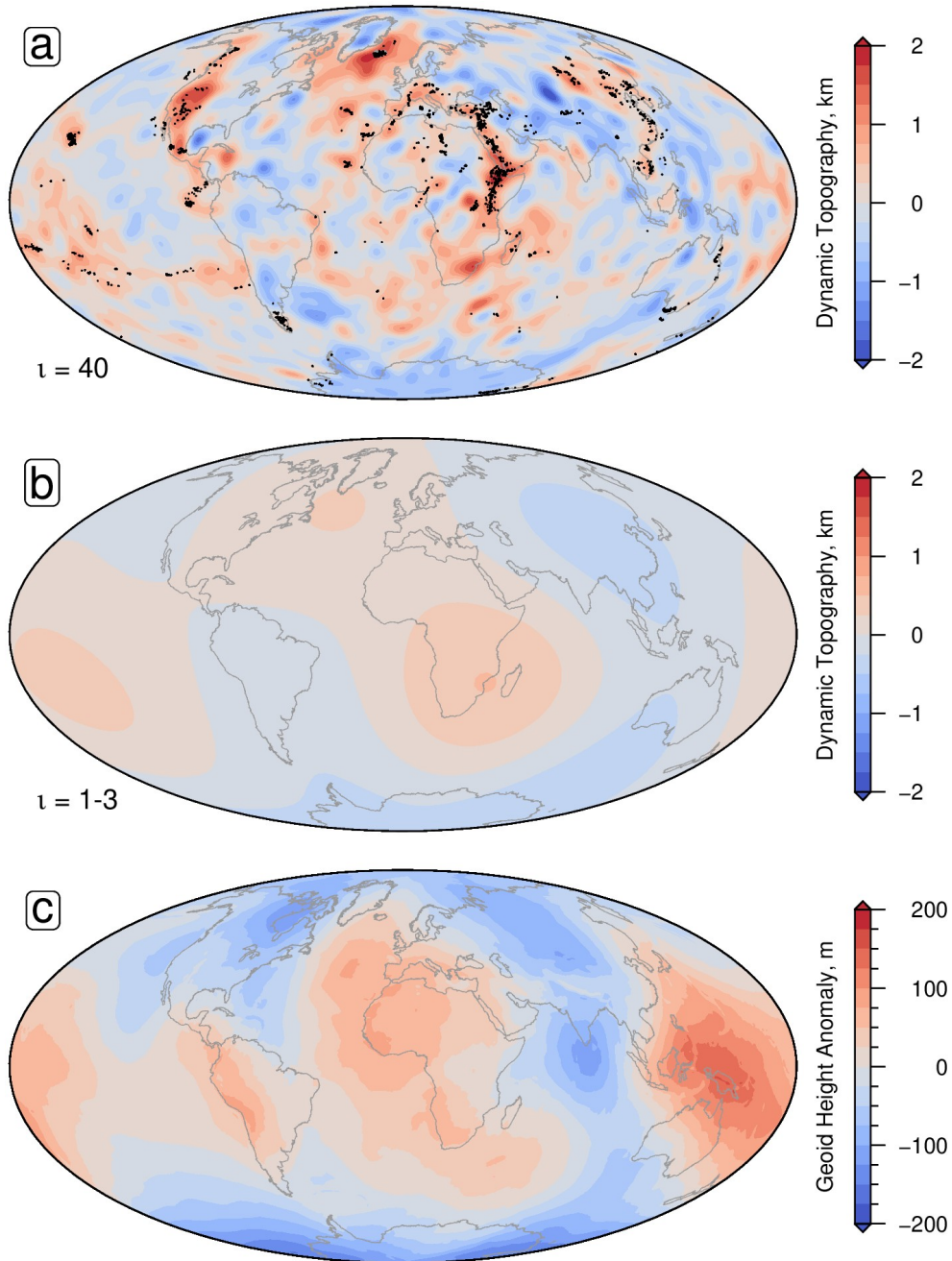


**Figure 16. Benchmarking of the spherical harmonic representation.** (a) Spherical harmonic representation of residual depth measurements at spherical harmonic degree  $l = 40$ . Black circles = Neogene-Quaternary intraplate volcanic rocks (Ball et al., 2021). (b) Spherical harmonic representation of residual depth measurements for spherical harmonic degree  $l = 1-3$ . (c) Geoid height anomaly (Chambat et al., 2010).

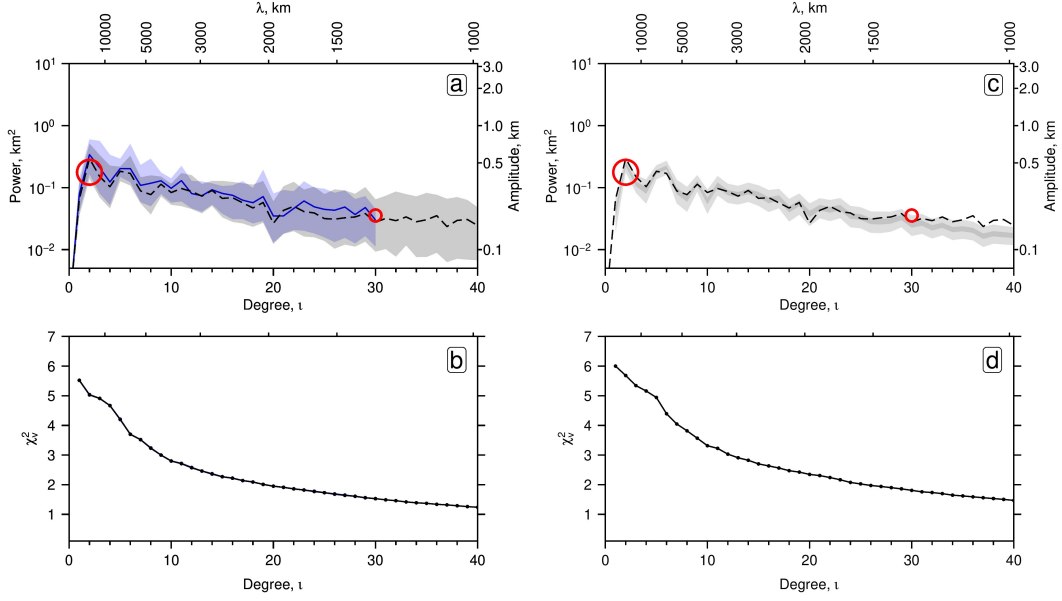


**Figure 17. Observed power spectra.** (a) Blue/gray lines with bands = power spectra out to  $l = 30/l = 40$  obtained by regularized least-squares inversion of global database shown in Figure 12 with uncertainties estimated from range of gradient regularization and amplitude damping coefficients ( $10^{0.5}$ – $10^{+0.5}$  and  $10^2$ – $10^3$ , respectively). Red circles = magnitudes of power at  $l = 2$  and  $l = 30$  taken from Hoggard et al. (2016) where diameter of circle is proportional to uncertainty. (b) Residual misfit,  $\chi_v^2$ , for  $l = 40$  plotted as function of spherical harmonic degree,  $l$ . (c) Pair of gray bands = power spectrum and its uncertainty out to  $l = 40$  obtained by Gaussian Process algorithm (Valentine & Davies, 2020). Dark and light bands = ranges spanned by central 50% and 99% of spectra computed for 100,000 random samples, respectively. Black dashed line = power spectrum out to  $l = 40$  taken from Panel (a) for comparison. (d) Residual misfit,  $\chi_v^2$ , for  $l = 40$  plotted as function of spherical harmonic degree,  $l$ .

**Table 1.** Symbols and values of parameters for calculating residual depth/topography.

Symbol	Parameter	Value	Units
$C$	Clay fraction	$0.5 \pm 0.25$	dimensionless
$C_c$	Correction due to oceanic crustal thickness	-	km
$C_{cc}$	Correction due to continental crustal thickness	-	km
$C_g$	Correction due to geoid	-	km
$C_s$	Correction due to sediment load	-	km
$\lambda$	Compaction decay length	2.3	km
$\phi$	Porosity	-	dimensionless
$\phi_o$	Porosity, initial	0.67	dimensionless
$\bar{\rho}_c$	Density of oceanic crust	-	$\text{Mg m}^{-3}$
$\bar{\rho}_{cc}$	Density of continental crust	-	$\text{Mg m}^{-3}$
$\bar{\rho}_{cr}$	Density of continental crust (mean)	$2.78 \pm 0.04$	$\text{Mg m}^{-3}$
$\rho_m$	Density of mantle at 0°C	$3.33 \pm 0.02$	$\text{Mg m}^{-3}$
$\rho_a$	Density of asthenospheric mantle	$3.20 \pm 0.02$	$\text{Mg m}^{-3}$
$\bar{\rho}_r$	Mean density of oceanic crust	$2.84 \pm 0.07$	$\text{Mg m}^{-3}$
$\bar{\rho}_s$	Mean density of local sediment	-	$\text{Mg m}^{-3}$
$\rho_{sg}$	Solid grain density	$2.65 \pm 0.05$	$\text{Mg m}^{-3}$
$\rho_w$	Density of seawater	$1.03 \pm 0.01$	$\text{Mg m}^{-3}$
$t$	Two-way travel time (TWTT)	-	s
$t_c$	Crustal thickness	-	s
$t_o$	Observed topography	-	km
$t_r$	Residual topography	-	km
$t_s$	Sediment thickness	-	s
$T_p$	Mantle potential temperature	$1326 \pm 50$	°C
$\bar{v}_p$	Bulk velocity of oceanic crust	-	$\text{km s}^{-1}$
$v_p$	P-wave velocity	-	$\text{km s}^{-1}$
$v_{sg}$	Acoustic velocity of solid grains	$4.50 \pm 0.50$	$\text{km s}^{-1}$
$v_w$	Acoustic velocity of pore fluid	$1.50 \pm 0.01$	$\text{km s}^{-1}$
$z$	Depth	-	km
$z_c$	Oceanic crustal thickness	-	km
$z_{cc}$	Continental crustal thickness	-	km
$\bar{z}_{cr}$	Continental crustal thickness (mean)	$32.35 \pm 5.96$	km
$z_o$	Depth to water-loaded basement (observed)	-	km
$z_p$	Plate thickness	$111 \pm 10$	km
$z_r$	Residual depth	-	km
$\bar{z}_r$	Oceanic crustal thickness (mean)	$6.38 \pm 1.12$	km
$z_{rd}$	Ridge depth	$2.92 \pm 0.5$	km
$z_s$	Sediment thickness	-	km
$z_{sb}$	Depth to the seabed	-	km
$z_w$	Depth to water-loaded basement (expected)	-	km

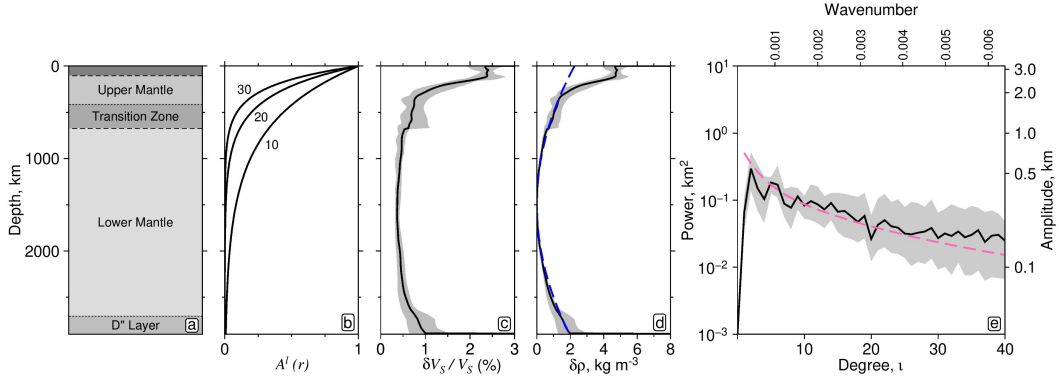


**Figure 18. Analytical power spectrum.** (a) Schematic mantle structure. (b) Normalized surface response kernels,  $A^l(r)$ , as function of depth approximated using exponential curves for  $l = 10, 20$  and  $30$ . (c) rms amplitude of relative perturbations of mantle shear wave velocity,  $\delta V_s / V_s$ , from six tomographic models (Ekström & Dziewonski, 1998; Ritsema et al., 1999; Masters et al., 2000; Mégnin & Romanowicz, 2000; Grand, 2002; Antolik et al., 2003). (d) Radial density anomaly,  $\delta \rho$ , as function of depth. Black line with gray band = average radial density anomaly relative to Preliminary Reference Earth Model (PREM) calculated from set of six shear wave tomographic models with one standard deviation (Forte, 2007; Dziewonski & Anderson, 1981). Blue dashed line = estimate of density anomaly where  $b = 1 \times 10^{-12} \text{ kg m}^{-5}$ . (e) Observed and calculated spectra. Black line with gray band = observed power spectrum and uncertainty obtained by regularized least-squares inversion of global database (see Figure 17a); pink dashed line = power spectrum calculated by solving Equation 19.

## References

766

767

768

769

770

771

772

773

774

775

776

777

778

779

780

781

782

783

784

785

786

787

788

789

790

791

792

793

794

795

796

797

798

799

800

801

802

803

804

805

806

807

808

809

810

811

812

813

814

815

816

817

818

819

- Airy, G. B. (1855). On the computation of the effect of the attraction of mountain-masses, as distributing the apparent astronomical latitude of stations in geodesic surveys. *Philosophical Transactions of the Royal Society*, *145*, 101–104.
- Al-Subbary, A.-K., Nichols, G. J., Bosence, D. W. J., & Al-Kadasi, M. (1998). Pre-rift doming, peneplanation or subsidence in the southern Red Sea? Evidence from the Medj-zir Formation (Tawilah Group) of western Yemen. *Sedimentation and Tectonics in Rift Basins Red Sea:- Gulf of Aden*(1992), 119–134. doi: 10.1007/978-94-011-4930-3\_8
- Amante, C., & Eakins, B. W. (2009). ETOPO1 1 Arc-Minute Global Relief Model: Procedures, Data Sources and Analysis. *NOAA Technical Memorandum NESDIS NGDC-24*.
- Antolik, M., Gu, Y. J., Ekström, G., & Dziewonski, A. M. (2003). J362D28: a new joint model of compressional and shear velocity in the Earth’s mantle. *Geophysical Journal International*, *153*(2), 443–466.
- Athy, L. F. (1930). Density, porosity, and compaction of sedimentary rocks. *AAPG Bulletin*, *14*(1), 1–24.
- Ball, P. W., White, N. J., MacLennan, J., & Stephenson, S. N. (2021). Global influence of mantle temperature and plate thickness on intraplate volcanism. *Nature communications*, *12*(1), 1–13.
- Benmansour, S., Andreu, B., & Yahiaoui, A. (2016). The Campanian-Maastrichtian of the Aures Basin, Algeria: Paleobiogeographical distribution of ostracods. *Cretaceous Research*, *58*, 86–107. Retrieved from <http://dx.doi.org/10.1016/j.cretres.2015.09.015> doi: 10.1016/j.cretres.2015.09.015
- Berggren, W. A. (1974). Paleocene Benthonic Foraminiferal Biostratigraphy, Biogeography and Paleoecology of Libya and Mali. *Micropaleontology*, *20*(4), 449. doi: 10.2307/1485130
- Carlson, R. L., & Herrick, C. N. (1990). Densities and porosities in the oceanic crust and their variations with depth and age. *Journal of Geophysical Research*, *95*(B6), 9153–9170. doi: 10.1029/JB095iB06p09153
- Castagna, J. P., Batzle, M. L., & Eastwood, R. L. (1985). Relationships between compressional-wave and shear-wave velocities in clastic silicate rocks. *geophysics*, *50*(4), 571–581.
- Chambat, F., Ricard, Y., & Valette, B. (2010). Flattening of the Earth: Further from hydrostaticity than previously estimated. *Geophysical Journal International*, *183*(2), 727–732. doi: 10.1111/j.1365-246X.2010.04771.x
- Christensen, N. I. (1965). Compressional wave velocities in metamorphic rocks at pressures to 10 kilobars. *Journal of Geophysical Research*, *70*(24), 6147–6164.
- Christensen, N. I. (1978). Ophiolites, seismic velocities and oceanic crustal structure. *Tectonophysics*, *47*(1-2), 131–157.
- Christensen, N. I., & Salisbury, M. H. (1975). Structure and constitution of the lower oceanic crust. *Reviews of Geophysics*, *13*(1), 57–86.
- Christeson, G. L., Goff, J. A., & Reece, R. S. (2019). Synthesis of Oceanic Crustal Structure From Two-Dimensional Seismic Profiles. *Reviews of Geophysics*, *57*(2), 504–529.
- Coffin, M. F., Duncan, R. A., Eldholm, O., Fitton, J. G., Frey, F. A., Larsen, H. C., ... Wallace, P. J. (2006). Large igneous provinces and scientific ocean drilling: Status quo and a look ahead. *Oceanography*, *19*(4), 150–160.
- Conway-Jones, B. W., Roberts, G. G., Fichtner, A., & Hoggard, M. (2019). Neogene epeirogeny of Iberia. *Geochemistry, Geophysics, Geosystems*, *20*(2), 1138–1163.
- Crosby, A. G., McKenzie, D. P., & Sclater, J. G. (2006). The relationship between depth, age and gravity in the oceans. *Geophysical Journal International*, *166*(2), 553–573. doi: 10.1111/j.1365-246X.2006.03015.x

- 820 Crough, S. T. (1983). The correction for sediment loading on the seafloor. *Journal of*  
821 *Geophysical Research: Solid Earth*, *88*(B8), 6449–6454.
- 822 Czarnota, K., Hoggard, M. J., White, N. J., & Winterbourne, J. (2013). Spatial  
823 and temporal patterns of Cenozoic dynamic topography around Australia.  
824 *Geochemistry, Geophysics, Geosystems*, *14*(3), 634–658.
- 825 Czarnota, K., Roberts, G. G., White, N. J., & Fishwick, S. (2014). Spatial and tem-  
826 poral patterns of Australian dynamic topography from River Profile Modeling.  
827 *Journal of Geophysical Research: Solid Earth*, *119*(2), 1384–1424.
- 828 Dalton, C. A., Langmuir, C. H., & Gale, A. (2014). Geophysical and geochemical  
829 evidence for deep temperature variations beneath mid-ocean ridges. *Science*,  
830 *344*(6179), 80–83.
- 831 Dziewonski, A. M., & Anderson, D. L. (1981). Preliminary reference Earth model.  
832 *Physics of the earth and planetary interiors*, *25*(4), 297–356.
- 833 Eberhart-Phillips, D., Han, D.-H., & Zoback, M. D. (1989). Empirical relation-  
834 ships among seismic velocity, effective pressure, porosity, and clay content in  
835 sandstone. *Geophysics*, *54*(1), 82–89.
- 836 Ekström, G., & Dziewonski, A. M. (1998). The unique anisotropy of the Pacific up-  
837 per mantle. *Nature*, *394*(6689), 168–172.
- 838 Forte, A. M. (2007). Constraints on seismic models from other disciplines-  
839 Implications for mantle dynamics and composition. *Treatise on Geophysics*, *1*,  
840 805–858.
- 841 Grand, S. P. (2002). Mantle shear-wave tomography and the fate of subducted  
842 slabs. *Philosophical Transactions of the Royal Society of London. Series A:*  
843 *Mathematical, Physical and Engineering Sciences*, *360*(1800), 2475–2491.
- 844 Grose, C. J., & Afonso, J. C. (2013). Comprehensive plate models for the thermal  
845 evolution of oceanic lithosphere. *Geochemistry, Geophysics, Geosystems*, *14*(9),  
846 3751–3778. doi: 10.1002/ggge.20232
- 847 Gunn, R. (1943). A quantitative evaluation of the influence of the lithosphere on the  
848 anomalies of gravity. *Journal of the Franklin Institute*, *236*(1), 47–66.
- 849 Hager, B. H., Clayton, R. W., Richards, M. A., Comer, R. P., & Dziewonski, A. M.  
850 (1985). Lower mantle heterogeneity, dynamic topography and the geoid. *Na-*  
851 *ture*, *313*(6003), 541–545.
- 852 Hager, B. H., & Richards, M. A. (1989). Long-wavelength variations in Earth’s  
853 geoid: physical models and dynamical implications. *Philosophical Transactions*  
854 *of the Royal Society of London. Series A, Mathematical and Physical Sciences*,  
855 *328*(1599), 309–327.
- 856 Han, D.-h., Nur, A., & Morgan, D. (1986). Effects of porosity and clay content on  
857 wave velocities in sandstones. *Geophysics*, *51*(11), 2093–2107.
- 858 Hasterok, D. (2013). Global patterns and vigor of ventilated hydrothermal circula-  
859 tion through young seafloor. *Earth and Planetary Science Letters*, *380*, 12–  
860 20. Retrieved from <http://dx.doi.org/10.1016/j.epsl.2013.08.016> doi:  
861 10.1016/j.epsl.2013.08.016
- 862 Hasterok, D., Chapman, D. S., & Davis, E. E. (2011). Oceanic heat flow: Implica-  
863 tions for global heat loss. *Earth and Planetary Science Letters*, *311*(3-4), 386–  
864 395. Retrieved from <http://dx.doi.org/10.1016/j.epsl.2011.09.044> doi:  
865 10.1016/j.epsl.2011.09.044
- 866 Herzberg, C., Asimow, P. D., Arndt, N., Niu, Y., Leshner, C. M., Fitton, J. G., ...  
867 Saunders, A. D. (2007). Temperatures in ambient mantle and plumes: Con-  
868 straints from basalts, picrites, and komatiites. *Geochemistry, Geophysics,*  
869 *Geosystems*, *8*(2). doi: 10.1029/2006GC001390
- 870 Hoggard, M. J., White, N. J., & Al-Attar, D. (2016). Global dynamic topogra-  
871 phy observations reveal limited influence of large-scale mantle flow. *Nature*  
872 *Geoscience*, *9*(6), 456–463. doi: 10.1038/ngeo2709
- 873 Hoggard, M. J., Winterbourne, J., Czarnota, K., & White, N. J. (2017). Oceanic  
874 residual depth measurements, the plate cooling model, and global dynamic

- 875 topography. *Journal of Geophysical Research: Solid Earth*, *122*(3), 2328–2372.  
876 doi: 10.1002/2016JB013457
- 877 Howie, R. A., Zussman, J., & Deer, W. (1992). *An introduction to the rock-forming*  
878 *minerals*. Longman London, UK.
- 879 Ji, S., Sun, S., Wang, Q., & Marcotte, D. (2010). Lamé parameters of common rocks  
880 in the Earth’s crust and upper mantle. *Journal of Geophysical Research: Solid*  
881 *Earth*, *115*(B6).
- 882 Jordan, T. H. (1975). The continental tectosphere. *Reviews of Geophysics*, *13*(3), 1–  
883 12.
- 884 Katsura, T., Yamada, H., Nishikawa, O., Song, M., Kubo, A., Shinmei, T., . . . Fu-  
885 nakoshi, K.-i. (2004). Olivine-wadsleyite transition in the system (Mg,Fe)  
886 2 SiO 4. *Journal of Geophysical Research: Solid Earth*, *109*(B2), 1–12. doi:  
887 10.1029/2003jb002438
- 888 Klöcking, M., White, N. J., Maclennan, J., McKenzie, D., & Fitton, J. G. (2018).  
889 Quantitative Relationships Between Basalt Geochemistry, Shear Wave Ve-  
890 locity, and Asthenospheric Temperature Beneath Western North Amer-  
891 ica. *Geochemistry, Geophysics, Geosystems*, *19*(9), 3376–3404. doi:  
892 10.1029/2018GC007559
- 893 Kowallis, B. J., Jones, L. E. A., & Wang, H. F. (1984). Velocity-porosity-clay con-  
894 tent systematics of poorly consolidated sandstones. *Journal of Geophysical Re-*  
895 *search: Solid Earth*, *89*(B12), 10355–10364.
- 896 Lambeck, K., Johnston, P., Smither, C., & Nakada, M. (1996). Glacial rebound of  
897 the British IslesIII. Constraints on mantle viscosity. *Geophysical Journal Inter-*  
898 *national*, *125*(2), 340–354.
- 899 Lee, C. T. A., Luffi, P., Plank, T., Dalton, H., & Leeman, W. P. (2009). Con-  
900 straints on the depths and temperatures of basaltic magma generation on  
901 Earth and other terrestrial planets using new thermobarometers for mafic  
902 magmas. *Earth and Planetary Science Letters*, *279*(1-2), 20–33. doi:  
903 10.1016/j.epsl.2008.12.020
- 904 Levitt, D. A., & Sandwell, D. T. (1995). Lithospheric bending at subduction zones  
905 based on depth soundings and satellite gravity. *Journal of Geophysical Re-*  
906 *search: Solid Earth*, *100*(B1), 379–400.
- 907 Loudon, K. E., Tucholke, B. E., & Oakey, G. N. (2004). Regional anomalies of sed-  
908 iment thickness, basement depth and isostatic crustal thickness in the North  
909 Atlantic Ocean. *Earth and Planetary Science Letters*, *224*(1-2), 193–211.
- 910 Luger, P. (2003). Paleobiogeography of late early cretaceous to early paleo-  
911 ocene marine ostracoda in Arabia and North to Equatorial Africa. *Palaeo-*  
912 *geography, Palaeoclimatology, Palaeoecology*, *196*(3-4), 319–342. doi:  
913 10.1016/S0031-0182(03)00462-0
- 914 Martill, D. M., Ibrahim, N., Brito, P. M., Baider, L., Zhou, S., Loveridge, R., . . .  
915 Hing, R. (2011). A new plattenkalk Konservat Lagerstätte in the Upper Cre-  
916 taceous of Gara Sbaa, south-eastern Morocco. *Cretaceous Research*, *32*(4),  
917 433–446.
- 918 Masters, G., Laske, G., Bolton, H., & Dziewonski, A. (2000). The relative behavior  
919 of shear velocity, bulk sound speed, and compressional velocity in the mantle:  
920 Implications for chemical and thermal structure. *Washington DC American*  
921 *Geophysical Union Geophysical Monograph Series*, *117*, 63–87.
- 922 Matthews, S., Shorttle, O., & Maclennan, J. (2016). The temperature of the Ice-  
923 landic mantle from olivine-spinel aluminum exchange thermometry. *Geochem-*  
924 *istry, Geophysics, Geosystems*, *17*(11), 4725–4752.
- 925 Maus, S., Barckhausen, U., Berkenbosch, H., Bournas, N., Brozina, J., Childers, V.,  
926 . . . Von Frese, R. R. B. (2009). EMAG2: A 2-arc min resolution Earth Mag-  
927 netic Anomaly Grid compiled from satellite, airborne, and marine magnetic  
928 measurements. *Geochemistry, Geophysics, Geosystems*, *10*(8).
- 929 McCartney, J. A., Roberts, E. M., Tapanila, L., & O’Leary, M. A. (2018). Large

- 930 palaeophiid and nigerophiid snakes from Paleogene Trans-Saharan Seaway  
 931 deposits of Mali. *Acta Palaeontologica Polonica*, *63*, 207–220.
- 932 McKenzie, D., Jackson, J., & Priestley, K. (2005). Thermal structure of oceanic and  
 933 continental lithosphere. *Earth and Planetary Science Letters*, *233*(3–4), 337–  
 934 349. doi: 10.1016/j.epsl.2005.02.005
- 935 McKenzie, D. P. (1967). Some remarks on heat flow and gravity anomalies. *Journal*  
 936 *of Geophysical Research*, *72*(24), 6261–6273. doi: 10.1029/jz072i024p06261
- 937 McNab, F., Ball, P. W., Hoggard, M. J., & White, N. J. (2018). Neogene Uplift  
 938 and Magmatism of Anatolia: Insights From Drainage Analysis and Basaltic  
 939 Geochemistry. *Geochemistry, Geophysics, Geosystems*, *19*(1), 175–213. doi:  
 940 10.1002/2017GC007251
- 941 Mégnin, C., & Romanowicz, B. (2000). The three-dimensional shear velocity  
 942 structure of the mantle from the inversion of body, surface and higher-mode  
 943 waveforms. *Geophysical Journal International*, *143*(3), 709–728.
- 944 Menard, H. W. (1973). Depth anomalies and the bobbing motion of drifting islands.  
 945 *Journal of Geophysical Research*, *78*(23), 5128–5137.
- 946 O’Malley, C. P., White, N. J., Stephenson, S. N., & Roberts, G. G. (2021). Large-  
 947 Scale Tectonic Forcing of the African Landscape. *Journal of Geophysical Re-*  
 948 *search: Earth Surface*, *126*(12), 1–37. doi: 10.1029/2021JF006345
- 949 Parsons, B., & Sclater, J. G. (1977). An analysis of the variation of ocean floor  
 950 bathymetry and heat flow with age. *Journal of Geophysical Research*, *82*(5),  
 951 803–827.
- 952 Petters, S. W. (1978). Mid-Cretaceous paleoenvironments and biostratigraphy of  
 953 the Benue Trough, Nigeria. *Geological Society of America Bulletin*, *89*(1), 151–  
 954 154.
- 955 Pratt, J. H. (1855). On the attraction of the Himalaya Mountains, and of the ele-  
 956 vated regions beyond them, upon the plumb-line in India. *Philosophical Trans-*  
 957 *actions of the Royal Society*, *145*, 53–100.
- 958 Priestley, K., & McKenzie, D. (2013). The relationship between shear wave veloc-  
 959 ity, temperature, attenuation and viscosity in the shallow part of the mantle.  
 960 *Earth and Planetary Science Letters*, *381*, 78–91.
- 961 Rasmussen, C. E., & Williams, C. K. I. (2006). *Gaussian processes for machine*  
 962 *learning*. Cambridge, USA: MIT Press.
- 963 Reyment, R. A., & Dingle, R. V. (1987). Palaeogeography of Africa during the  
 964 Cretaceous period. *Palaeogeography, Palaeoclimatology, Palaeoecology*, *59*, 93–  
 965 116.
- 966 Richards, F. D., Hoggard, M. J., Cowton, L. R., & White, N. J. (2018). Reassessing  
 967 the Thermal Structure of Oceanic Lithosphere With Revised Global Invento-  
 968 ries of Basement Depths and Heat Flow Measurements. *Journal of Geophysical*  
 969 *Research: Solid Earth*, *123*(10), 9136–9161. doi: 10.1029/2018JB015998
- 970 Richards, F. D., Hoggard, M. J., White, N., & Ghelichkhan, S. (2020). Quanti-  
 971 fying the Relationship Between Short-Wavelength Dynamic Topography and  
 972 Thermomechanical Structure of the Upper Mantle Using Calibrated Param-  
 973 eterization of Anelasticity. *Journal of Geophysical Research: Solid Earth*,  
 974 *125*(9). doi: 10.1029/2019JB019062
- 975 Richards, M. A., & Hager, B. H. (1984). Geoid anomalies in a dynamic earth.  
 976 *Journal of Geophysical Research*, *89*(B7), 5987–6002. doi: 10.1029/  
 977 JB089iB07p05987
- 978 Ritsema, J., Deuss, a. A., Van Heijst, H. J., & Woodhouse, J. H. (2011). S40RTS: a  
 979 degree-40 shear-velocity model for the mantle from new Rayleigh wave disper-  
 980 sion, teleseismic traveltimes and normal-mode splitting function measurements.  
 981 *Geophysical Journal International*, *184*(3), 1223–1236.
- 982 Ritsema, J., van Heijst, H. J., & Woodhouse, J. H. (1999). Complex shear wave ve-  
 983 locity structure imaged beneath Africa and Iceland. *Science*, *286*(5446), 1925–  
 984 1928.

- 985 Roberts, G. G., White, N., Hoggard, M. J., Ball, P. W., & Meenan, C. (2018). A  
 986 Neogene history of mantle convective support beneath Borneo. *Earth and*  
 987 *Planetary Science Letters*, *496*, 142–158. Retrieved from [https://doi.org/](https://doi.org/10.1016/j.epsl.2018.05.043)  
 988 [10.1016/j.epsl.2018.05.043](https://doi.org/10.1016/j.epsl.2018.05.043) doi: 10.1016/j.epsl.2018.05.043
- 989 Rodríguez Tribaldos, V., White, N. J., Roberts, G. G., & Hoggard, M. J. (2017).  
 990 Spatial and temporal uplift history of South America from calibrated  
 991 drainage analysis. *Geochemistry, Geophysics, Geosystems*, *18*(6), 2321–2353.
- 992 Rowley, D. B. (2019). Oceanic axial depth and age-depth distribution of oceanic  
 993 lithosphere: Comparison of magnetic anomaly picks versus age-grid models.  
 994 *Lithosphere*, *11*(1), 21–43. doi: 10.1130/L1027.1
- 995 Sahagian, D. (1988). Epeirogenic motions of Africa as inferred from Cretaceous  
 996 shoreline deposits. *Tectonics*, *7*(1), 125–138.
- 997 Sandwell, D. T., Müller, R. D., Smith, W. H., Garcia, E., & Francis, R. (2014).  
 998 New global marine gravity model from CryoSat-2 and Jason-1 reveals buried  
 999 tectonic structure. *Science*, *346*(6205), 65–67. doi: 10.1126/science.1258213
- 1000 Schaeffer, A. J., & Lebedev, S. (2013). Global shear speed structure of the upper  
 1001 mantle and transition zone. *Geophysical Journal International*, *194*(1), 417–  
 1002 449. doi: 10.1093/gji/ggt095
- 1003 Seton, M., Müller, R. D., Zahirovic, S., Williams, S., Wright, N. M., Cannon, J., ...  
 1004 McGirr, R. (2020). A Global Data Set of Present-Day Oceanic Crustal Age  
 1005 and Seafloor Spreading Parameters. *Geochemistry, Geophysics, Geosystems*,  
 1006 *21*(10), 1–15. doi: 10.1029/2020gc009214
- 1007 Stein, C. A., & Stein, S. (1992). A model for the global variation in oceanic depth  
 1008 and heat flow with lithospheric age. *Nature*, *359*(6391), 123–129.
- 1009 Steinberger, B., Werner, S. C., & Torsvik, T. H. (2010). Deep versus shallow origin  
 1010 of gravity anomalies, topography and volcanism on Earth, Venus and Mars.  
 1011 *Icarus*, *207*(2), 564–577.
- 1012 Stephenson, S., Hoggard, M., & White, N. (2021). Global Continental Residual To-  
 1013 pography. In *Egu general assembly conference abstracts* (pp. EGU21–15505).
- 1014 Stephenson, S. N., White, N. J., Carter, A., Seward, D., Ball, P. W., & Klöcking,  
 1015 M. (2021). Cenozoic dynamic topography of Madagascar. *Geochemistry,*  
 1016 *Geophysics, Geosystems*, *22*(6), e2020GC009624.
- 1017 Stierman, D. J., Healy, J. H., & Kovach, R. L. (1979). Pressure-induced velocity gra-  
 1018 dient: An alternative to a Pg refractor in the Gabilan range, central California.  
 1019 *Bulletin of the Seismological Society of America*, *69*(2), 397–415.
- 1020 Straume, E. O., Gaina, C., Medvedev, S., Hochmuth, K., Gohl, K., Whittaker,  
 1021 J. M., ... Hopper, J. R. (2019). GlobSed: Updated Total Sediment Thick-  
 1022 ness in the World’s Oceans. *Geochemistry, Geophysics, Geosystems*, *20*(4),  
 1023 1756–1772. doi: 10.1029/2018GC008115
- 1024 Sykes, T. J. S. (1996). A correction for sediment load upon the ocean floor: Uni-  
 1025 form versus varying sediment density estimations-Implications for isostatic  
 1026 correction. *Marine Geology*, *133*(1-2), 35–49.
- 1027 Tapanila, L., Roberts, E. M., Bouaré, M. L., Sissoko, F., & O’Leary, M. A. (2008).  
 1028 Phosphate taphonomy of bone and coprolite conglomerates: a case study from  
 1029 the Eocene of Mali, NW Africa. *Palaios*, *23*(3), 139–152.
- 1030 Tesauro, M., Kaban, M. K., & Cloetingh, S. A. (2012). Global strength and elastic  
 1031 thickness of the lithosphere. *Global and Planetary Change*, *90-91*, 51–57. Re-  
 1032 trieved from <http://dx.doi.org/10.1016/j.gloplacha.2011.12.003> doi:  
 1033 [10.1016/j.gloplacha.2011.12.003](https://doi.org/10.1016/j.gloplacha.2011.12.003)
- 1034 Tosaya, C., & Nur, A. (1982). Effects of diagenesis and clays on compressional veloci-  
 1035 ties in rocks. *Geophysical Research Letters*, *9*(1), 5–8.
- 1036 Valentine, A. P., & Davies, D. R. (2020). Global Models From Sparse Data: A Ro-  
 1037 bust Estimate of Earth’s Residual Topography Spectrum. *Geochemistry, Geo-*  
 1038 *physics, Geosystems*, *21*(8), 1–19. doi: 10.1029/2020GC009240
- 1039 Von Herzen, R. P., & Uyeda, S. (1963). Heat flow through the eastern Pacific ocean

- 1040 floor. *Journal of Geophysical Research*, 68(14), 4219–4250. doi: 10.1029/  
 1041 JZ068i014p04219
- 1042 Watts, A. B. (2001). *Isostasy and Flexure of the Lithosphere*. Cambridge University  
 1043 Press.
- 1044 Watts, A. B., & Zhong, S. (2000). Observations of flexure and the rheology of  
 1045 oceanic lithosphere. *Geophysical Journal International*, 142(3), 855–875. doi:  
 1046 10.1046/j.1365-246X.2000.00189.x
- 1047 White, R. S., McKenzie, D. a. N., & Nions, K. O. (1992). Oceanic crustal thickness  
 1048 from seismic measurements and rare earth element inversions. *Journal of Geo-*  
 1049 *physical Research*, 97(B13), 19,683–19,715. doi: 10.1016/j.csda.2008.03.004
- 1050 Wilson, J. W. P., Roberts, G. G., Hoggard, M. J., & White, N. J. (2014). Cenozoic  
 1051 epeirogeny of the Arabian Peninsula from drainage modeling. *Geochemistry,*  
 1052 *Geophysics, Geosystems*, 15(10), 3723–3761.
- 1053 Wilson, M. E., Chambers, J. L., Evans, M. J., Moss, S. J., & Nas, D. S. (1999).  
 1054 Cenozoic carbonates in Borneo: Case studies from northeast Kalimantan.  
 1055 *Journal of Asian Earth Sciences*, 17(1-2), 183–201. doi: 10.1016/  
 1056 S0743-9547(98)00045-2
- 1057 Winterbourne, J., Crosby, A. G., & White, N. J. (2009). Depth, age and dy-  
 1058 namic topography of oceanic lithosphere beneath heavily sedimented At-  
 1059 lantic margins. *Earth and Planetary Science Letters*, 287(1-2), 137–151.  
 1060 Retrieved from <http://dx.doi.org/10.1016/j.epsl.2009.08.019> doi:  
 1061 10.1016/j.epsl.2009.08.019
- 1062 Wyllie, M. R. J., Gregory, A. R., & Gardner, L. W. (1956). Elastic wave velocities  
 1063 in heterogeneous and porous media. *Geophysics*, 21(1), 41–70.
- 1064 Yamauchi, H., & Takei, Y. (2016). Polycrystal anelasticity at nearsolidus tempera-  
 1065 tures. *Journal of Geophysical Research: Solid Earth*, 121(11), 7790–7820.